# Progressive alignment of basal bodies in multiciliated cell: Dynamic motion of basal bodies revealed by long-term live imaging

多繊毛細胞における繊毛基底小体の配列形成：
長時間ライブイメージングによるダイナミクス解析

PhD Thesis

ELISA HERAWATI

**Laboratory of Biological Science**

**Graduate School of Frontier Bioscience**

**Osaka University**

# TABLE OF CONTENTS

# ACKNOWLEDGEMENTS

My deep gratitude goes first to my laboratory colleagues Kanoh Hatsuho, Kazuhiro Tateishi, and Yuki Ogura who shared the excitement of MTECs experiments.

My appreciation also extends to Daisuke Taniguchi and Shuji Ishihara from Meiji University for two years of collaborative research.

I am also grateful to Atsushi Tamura, Tomoki Yano, Shuhei Chiba for helpful discussions and persistent help. Thanks also goes to Masami Uji, Tomoki Nishida, and Fumiko Takenaga for technical assistance in our laboratory. I appreciate the critical technical assistance of H. Miyagi, H. Takatsuka, and A. Motomura (Olympus, Co. Ltd). I also thank Hidetaka Shiratori and Prof. Hiroshi Hamada for technical advice.

Above all, I would not have reached this stage without guidance of my supervisor Prof. Sachiko Tsukita. Her encouragement has been especially valuable through my graduate education.

Osaka, August 22, 2016

# List of Figures

# List of Abbreviations

| | |
|---|---|
| **ALI** | air-liquid interface |
| **BB** | basal body |
| **BF** | basal foot |
| **HMM** | heavy meromyosin |
| **IF** | intermediate filament |
| **MCC** | multiciliated cell |
| **MT** | microtubule |
| **MTEC** | mouse tracheal epithelial cell |
| **PCP** | planar cell polarity |
| **UHVEMT** | ultra-high voltage electron microscopic tomography |

# List of Appendixes

# Abstract

Multiciliated cells (MCCs) promote fluid flow through coordinated ciliary beating, which requires properly organized basal bodies (BBs). Airway MCCs have large numbers of BBs, which are uniformly oriented and, as shown here, aligned linearly. The mechanism for BB alignment is unexplored. A long-term and high resolution live cell imaging was developed and used to investigate the spatiotemporal dynamic of BBs during differentiation of MCCs in cultured mouse tracheal epithelial cells (MTECs). During MCC differentiation, the BB array adopted four stereotypical patterns, from a clustering "Floret" pattern to the linear "Alignment". This alignment process was correlated with BB orientations, revealed by double-immunostaining for BBs and their asymmetrically associated basal feet (BFs), indicating the possibility that ciliary alignment (BB alignment) stabilized the unidirectionality of the BBs to enhance the function of MCCs. The BB alignment was disrupted by disturbing apical microtubules with nocodazole and by a BF-depleting Odf2 mutation suggesting that interactions between components of the apical cytoskeleton and BBs were crucial for establishing and maintaining these ciliary patterns. This study highlights a possible biological function of the apical cytoskeleton in tracheal MCCs in the linear alignment of cilia.

# Chapter I. INTRODUCTION

## 1. Background

The formation of mature epithelial sheets involves multiple steps, in which epithelial cells adhere to each other to form a tight junction-based paracellular barrier, become polarized, and subsequently take on more specific differentiation states, as they adopt the highly ordered structures required to elicit specific biological functions in vertebrates (Guillot and Lecuit, 2013; Rodriguez-Boulan and Macara, 2014; Tamura and Tsukita, 2014). How such complex processes are regulated is a fundamental problem in cell biology and developmental biology.

Multiciliated cells (MCCs) are uniquely polarized to drive fluid transport in tissues by the synchronous beating and metachronal waves of hundreds of motile cilia on the apical membrane (Guirao and Joanny, 2007; Elgeti and Gompper, 2013). A differentiating MCC contains hundreds of basal bodies (BBs), which are short cylindrical structures at the base of mature cilia, and are docked at the apical membrane (Anderson, 1972; Satir and Dirksen, 2011). In most types of MCCs, the orientation of the BBs, identified by their asymmetrically associated basal feet (BFs), is precisely coordinated to support efficient mucociliary transport (Kunimoto et al., 2012; Chien et al., 2013).

The positional distribution of BBs (BB array) in the apical plane of MCCs depends on the cell type. For example, the BBs of ependymal MCCs in the brain exhibit unipolar clustering in the apical plane (Mirzadeh et al., 2010), while those of *Xenopus* larval skin MCCs are evenly distributed throughout the entire apical region (Werner et al., 2011; Turk et al., 2015). Cytoskeletons are involved in regulating these systems, in which microtubules (MTs) are thought to synchronize BB orientation downstream of the planar cell polarity (PCP) core-protein functions (Vladar et al., 2012). Sub-apical actin is required for the proper distance between neighboring BBs (Werner et al., 2011), and myosin II activity plays a role in the unipolar migration of BB clusters (Hirota et al., 2010). However, the mechanisms involved in correctly assembling and maintaining the proper distribution of BBs on the cell surface remain to be fully elucidated.

## 2. Statement of the problem

How multiciliated basal bodies are highly polarized after docking to the apical

membrane needs further clarification. Especially, the spatiotemporal information on the cellular process remains largely unknown. In the present study, mouse tracheal MCCs was examined in which the BBs are linearly aligned, a pattern also found in oviduct MCCs. This striking pattern prompted me to address the mechanism by which these BBs become regularly aligned in the apical membrane.

## 3. Objective

By employing a newly developed long-term live imaging method, this study focuses on the cellular process how basal bodies of multiciliated cell achieve their alignment pattern. This study is also aimed at elucidating the underlying mechanism of basal body alignment.

## Chapter II. LITERATURE REVIEW

### 1. Basal bodies in airway multiciliated cells

#### 1.1. Structure

In the airway system, motility of cilia wave mucus and debris upward the respiratory tree, in order to protect the lung from infection or irritation by pathogen. Cilia appears as hair-like projection ~10-15 μm long on the surface of some cells for movements of substance across the cell surface (Fig. 1 A). Each cilium is anchored at the cell surface by a modified centriole know as basal body (Fig 1 B). Basal body extends axoneme, membrane bound cylindrical structure, to the extracellular space. Basal bodies are distinguished from daughter centrioles by the presence of some appendages, including a basal foot, rootlet, distal appendages and sub distal appendages. Multiciliated cells basal bodies are not physically associated with daughter centrioles, although the daughter centrioles have crucial roles in the generation of the many basal bodies possessed by these cells (Satir and Christensen, 2007; Ishikawa and Marshall, 2011).

Besides anchoring axonemal cilia, basal bodies are associated with microtubule-organizing center activity. Many microtubules minus-end are found to be anchored via pericentriolar materials which surrounds basal body, or directly anchored via subdistal appendages protein such as Ninein and Dynactin complex (Moritz et al., 1995; Quintyne et al., 1999; Delgehyr et al., 2005). Since multiciliated cells are typical of terminally differentiated cells, they possess basal bodies during their entire lifetimes.

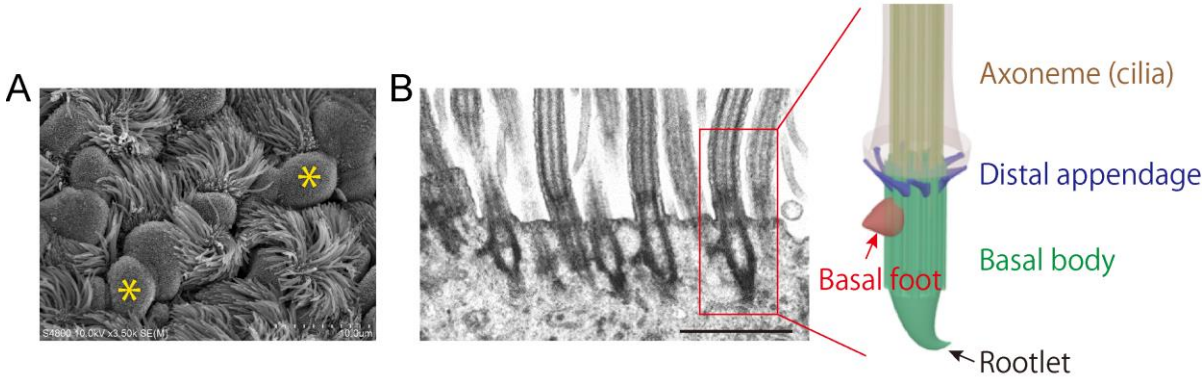


**Figure 1. Airway multiciliated cells**. (A) Scanning electron micrograph of luminal surface of mouse trachea. Hundreds of cilia project from multiciliated cells. Note that multiciliated cells are interspersed with other type of non-ciliated cells (secretory cells; asterisks). (B) Transmission electron micrograph of longitudinal thin-section across the cilia and the basal bodies (left). Cartoon of the basal body is drawn from inset (right). Bars, 10 μm (A); 500 nm (B).

### 1.2. Basal body generation, migration, and docking to the apical membrane

Generation of hundreds of basal bodies in multiciliated vertebrate cells occurs in the cytoplasma. Electron microscopic work in various multiciliated tissues including the *Xenopus* epidermis, the mammalian lung, and the avian trachea and oviduct have provided initial insight into the mechanism of this process (Steinman, 1968; Dirksen, 1971; Gordon, 1982, Boisvieux-Ulrich, 1985). While generation of multiple basal bodies occurs via mother centriole dependent pathway, ~90% of the total number of basal bodies are not templated by existing centrioles, but rather by an amorphous dense structure called "deuterosome" (Sorokin, 1968). Recent observation through live imaging showed that it is the daughter centriole, not the mother centriole, that contributes to formation of the deuterosome (Al Jord, 2014).

Following centriole formation in the cytoplasm, the future basal bodies must be transported to the apical surface of a MCC. Subsequently, basal body acquired accessories (distal appendage) to dock and then initiate cilia assembly (Hoyer-Fender, 2010; Kobayashi and Dynlacht, 2011). Transport of the nascent basal bodies to the apical cell membrane requires an intact actin cytoskeleton and involves actin-myosin-based mechanisms. Further elucidation of the role for actin networks in basal body docking revealed that basal body and actin network connection is mediated by Focal Adhesion Kinase (FAK). Knock down of FAK results in failure of apical basal body migration (Antoniades et al., 2014). Other molecular mechanism regulating network of actin filaments, and the assembly of this network involves actin regulators such as RhoA and the phosphate loop ATPase Nubp1 (Ioannou et al., 2013). The process of basal body docking modifies the formation of the apical actin network, and defects that impair docking are often associated with a thinner cortical actin network (Antoniades et al., 2014).

## 2. Control of basal body polarity

Polarization of cilia is another key aspect for functional cilia. A complex array of planar polarization events emerges after basal body docking, including those that determine basal body distance relative to their neighbors (spacing), their distribution relative to the surface area of the plasma membrane (translational polarity), and their orientation relative to external cues such as fluid flow and PCP (rotational polarity).

Within a single cell, cilia are oriented in the same direction, termed as rotational polarity (Marshall, and Kintner, 2008; Wallingford, 2010). Rotational polarity was established in a gradual manner, starting from weak polarization with many axonemes oriented more randomly. In the later developmental stage of MCC, mature axoneme undergo progressive refinement of their orientation (Boisvieux-Ulrich, 1985). Rotational polarity ensures cilia to beat coordinately in a synchronized and polarized fashion to effectively generate directional fluid flow (Marshall, and Kintner, 2008; Wallingford, 2010).

Control of rotational polarity is achieved through several mechanisms, such as positive feedback mechanism of fluid flow, cytoskeletal network, and planar cell polarity protein (Shimada et al., 2006; Park et al., 2008; Mitchell et al., 2009; Vladar et al., 2012). The role of positive feedback mechanism was first demonstrated in Xenopus study, where the weak but directional bias of flow of early immature axoneme direct reinforcement of cilia to correct the orientation (Mitchell at al., 2007). Such a feedback mechanism was also observed in MCCs of mouse brain ependymal cells, but not in tracheal MCC from the same species (Guirao et al., 2010; Matsuo et al., 2013). Thus, it seems that main regulatory control for cilia orientation, although it might share similar fundamental mechanism, it could be cell type specific.

Cytoskeletal organization is also a key regulator of cilia polarity in MCCs within a single cell. Besides its role for basal body docking, actin is also known as to maintain basal body array by forming proper distance between each basal bodies. Perturbation of actin leads to reduce in metachronal wave of cilia beating and cilia exhibits biased polarity but failed to undergo further refinement (Werner et al., 2011). In contrast, perturbation of microtubules leads to disruption of local polarity; neighboring cilia are oriented randomly with respect to one another. Recent studies by Vladar et al. revealed observation of prominent asymmetric microtubules which is enriched at proximal side of MCCs. In the absence of PCP signaling, the asymmetric accumulation of microtubules diminished, suggesting that enrichment of asymmetric microtubules is directed downstream of PCP proteins. Mutation of Vangl, one of core PCP protein, leads to defect of cilia polarization of the entire tissue. Other studies support the concept that PCP is the excellent candidate of upstream control of cytosketal polarity. Frz, Celsr2, and Celsr3 control the rotational polarity of basal bodies in MCCs (Seifert and Mlodzik,

2007; Park et al., 2008).

## 3. Physiology of ciliary beating and disease associated with cilia dysfunction

Beating of cilia consists of two phases: the effective stroke and the recovery stroke (Brooks and Wallingford, 2014). Each cycle begins with recovery stroke where cilia bends and largely parallel to the cell body, followed by fast effective stroke (forward). Because cilia generally act in aqueous environment, they are subjected to hydrodynamic consideration where fluid flow mediates interaction between neighboring cilia (Gueron et al., 1997). These interactions are thought as the basis of metachornal wave where cilia act cooperatively to produce a population level effect. The net result of this process is a traveling wave of ciliary action across the array that are essential for mucus transport and airway clearance (Wanner et al., 1996).

Inability to generate effective mucociliary transport causes chronic airway diseases, manifested by recurrent lung infection, coughing, sneezing, such as that shown in patient with primary ciliary dyskinesia (Leigh et al., 2007). Airway cilia from such patients often characterized by abnormal ultrastructure, such as absence of some or all dynein arms, radial spoke defects, absence of ciliary accessory resulting in aberrant beating pattern. Previous study in our laboratory has highlighted the importance of basal feet for functional mucociliary transport (Kunimoto et al., 2012). The authors found that basal feet are required for coordinated ciliary beating; basal bodies in the Odf2 mutant mice lacked basal feet and were incapable of undergoing rotational polarization, even in the presence of appropriate PCP cues. Normal microtubules lattice which commonly present in the wild type littermates was also disrupted in these mutant mice (Fig. 2). Phenotype associated to BB defect in Odf2 mutant mice include abnormal mucociliary clearance in the respiratory system, impaired hearing, and infertility in the female mice.

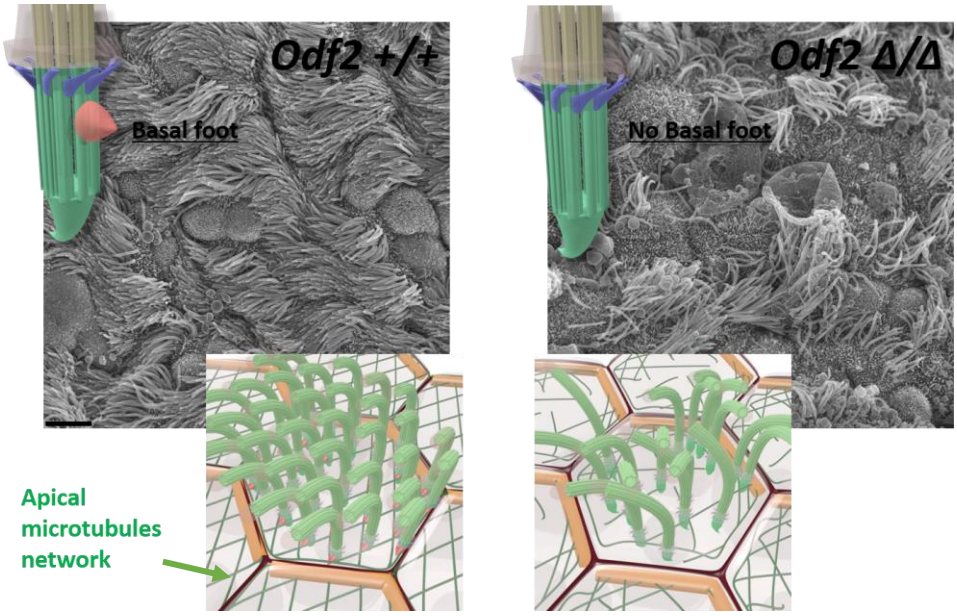


**Figure 2. Coordinated ciliary beating is disrupted in Odf2 mutant mouse which lack the basal feet structure**. Aberrant cilia organization is prominent in the mutant mouse. In a single cell, ciliary tufts are pointed in a random direction (right). The mutant mouse also displays poor network of apical MTs associated with basal bodies (cartoon; bottom). Original images were published in Kunimoto et al., 2012.

## Chapter III. METHODOLOGY

### 1. Animals

All procedures involving animals were approved by the institutional animal care and use committee of Osaka University. The mice used in this study included GFP-centrin2 (Higginbotham et al., 2004), wild type C57BL/6J (CLEA Japan), and *Odf2*$^{\Delta Ex6,7/\Delta Ex6,7}$GFP-centrin2. To generate *Odf2*$^{\Delta Ex6,7/\Delta Ex6,7}$GFP-centrin2 mice, homozygous GFP-centrin2 mice were crossed with *Odf2*$^{flox/+}$ mice to produce male *Odf2*$^{flox/+}$ GFP-centrin2 mice. Then, the latter were intercrossed with female CAG$^{Cre/+}$; *Odf2* $^{flox\text{-}del/+}$ mice to generate *Odf2*$^{\Delta Ex6,7/\Delta Ex6,7}$GFP-centrin2 mice. The protocols for genotyping were described previously (Kunimoto et al., 2012).

### 2. Primary culture of tracheal cells and long-term live imaging

MTEC cultures were prepared from the trachea of mice at 7-10 weeks of age as described previously (You et al., 2002), with replacement of the conventional medium. To improve the cell yield, enzymatic digestion was performed with gentle shaking at 4°C for 16-20 h. This method routinely yielded ~$1.08\times10^6$ cells/ml from 4 mice, which was sufficient for 20 Transwell 24-well filters (Corning). The enzymatic digestion was stopped by adding fetal bovine serum (FBS) (Cell Culture Bioscience) to the cell suspension at a final concentration of 10%. Cells were pooled by centrifugation at 400 *g* for 10 min at 4°C, then resuspended in MTEC Basic Medium (You et al., 2002) with 10% FBS for 3.5 h at 37°C, 5% $CO_2$ to adhere contaminating fibroblasts. Non-adherent cells were then collected by centrifugation, counted, and seeded at $10^5$cells/cm$^2$ onto polyester (PET) Transwell filters (Corning) coated with 50 μg/ml Collagen Type-I (Corning). The proliferation stage was maintained using the commercially available BEGM BulletKit (CC-3170, Lonza). The air liquid interface (ALI) stage was created after 4 days of culture using PneumaCult (05001, STEMCELL Technologies) according to the manufacturer's instructions. For live imaging, Transwell filters with a MTEC sheet (ALI 5-6 days) were cut out from the plastic support and inverted (cell side facing down) onto a glass-bottomed dish (D11140H, Matsunami Glass). Medium was supplied from an additional chamber attached to the back surface of the inverted insert. The medium was changed every other day.

### 3. Inhibitor experiments and HMM treatment

Inhibitor experiments were performed either during live imaging or under normal incubation conditions. For MT depolymerization, 6.6 μM nocodazole (Sigma) was applied to MTECs at ALI 6 days for 2 h, then replaced with 500 μl of fresh medium for recovery. For actin depolymerization, 10 μM cytochalasin D (Sigma) was used at ALI 7 days for 5-10 h.

To permit HMM to diffuse into the cells, MTECs at ALI 28 days were incubated with 0.1% TritonX-100/0.01 μM paclitaxel in PHEM buffer (60 mM PIPES [pH 6.9], 25 mM Hepes [pH 6.9], 10 mM EGTA, and 2 mM $MgCl_2$) for 15 min, then washed with PHEM buffer. Freshly thawed rabbit HMM solution was dialyzed against PHEM buffer at a final concentration of 1 mg/ml. The cells were then incubated with this HMM solution and 0.01 μM paclitaxel for 1 h at room temperature (RT), washed, and fixed for thin section electron microscopy.

### 4. Indirect immunofluorescence

MTECs and whole-mount trachea and oviduct were fixed in cold methanol (-20°C) or 4% paraformaldehyde (PFA) in Hepes buffered saline (RT), permeabilized with 0.2% Triton X-100/PBS for 5 min (RT), and then incubated in 1% BSA/PBS for 30 min (RT). Incubations with primary and secondary antibodies were carried out for 1 h each (RT). The following primary antibodies were used: rabbit anti-Odf2/Cenexin (1:500; Abcam), mouse anti-α-tubulin (1:500; Sigma), rabbit anti-Vangl1 (1:500; Sigma), rabbit anti-ZO-1 (1:500; Zymed), rat anti-Odf2 (Tateishi et al., 2013), rat anti-centriolin (Ishikawa et al., 2005), mouse anti-ZO-1 (T8-754) (Kitajiri et al., 2004), rabbit anti-plectin1 (1:100; Abcam), and mouse anti-keratin 8 (kindly provided by Drs. Y. Hirako and K. Owaribe, Nagoya University, Nagoya, Japan) antibodies. Secondary antibodies (1:500) included rat anti-GFP (Invitrogen) and species-specific AlexaFluor 488, 568, and 647 (Invitrogen) antibodies. Rhodamin-conjugated phalloidin was purchased from Invitrogen.

### 5. Lentivirus construction and production

To generate pLV-CAG1.1-tagRFPt vector, EGFP sequence of pLV-CAG1.1-EGFP vector (a kind gift from Masahito Ikawa, Osaka University, Osaka, Japan) were replaced by tagRFPt sequence flanked with *BamHI* and *SalI*. Total RNA from mouse

trachea was isolated using an RNAeasy mini kit (Qiagen) following the manufacturer's instructions. Reverse transcription was performed with a SuperScript II Reverse Transcriptase (Life Technologies). To generate pLV-CAG1.1-Centriolin-TagRFPt, two cDNA fragments (CentriolinN: 1-2845bp and CentriolinC: 2845-7612bp) encoding mouse Centriolin (available from GeneBank/EMBL/DDBJ under accession no. NM=012018.2) were amplified by PCR primers (for CentriolinN: 5'-gtcgacatgaagaaaggttctgaacgaag-3' and 5'-gccagaattctttccttctcttcatctgc-3', for CentriolinC: 5'-gaattctggcccaactccaggagtt-3' and 5'-gtcgacttagtggcggtaactgtttg-3') and then subcloned into pGEM-T-easy (Promega). CentriolinN and CentriolinC were simultaneously incorporated into *SalI*-digested pLV-CAG1.1-tagRFPt vector as a *SalI-EcoRI* or *EcoRI-SalI* fragment. The 2nd generation packaging plasmids (psPAX2 and pMD2.G) were provided from Yoshihide Tsujimoto (Osaka Univeristy, Osaka, Japan).

Lentiviral production was carried out as described previously (Vladar, 2007). Briefly, 10 cm dish cultured Lenti-X 293T cells (Clontech) were co-transfected with 2 μg pLV-CAG1.1-Centriolin-tagRFPt, 3.2 μg packaging plasmid (psPAX2) and 0.8 μg envelope plasmid (pMD2.G) using FuGENE HD (Promega). The lentiviral supernatant was harvested 48 h after transfection, and filtered through a 0.45-μm Millex®-HP (Merck Milipore). Following overnight PEG precipitation (4°C), the supernatant was concentrated by centrifugation at 1,500*g* for 30 min at 4°C. To infect MTECs at proliferation stage (70% confluency), tracheal cells were seeded one day prior to infection. Lentiviral supernatant was mixed with medium at the top of chamber, and then MTECs were further incubated at 37°C for 24 h. In the next day, fresh medium was supplied to the top and bottom chamber, and cells were continuously grown until assayed for live imaging.

## 6. Microscopy

### 6.1. Live imaging and super resolution confocal microscopy.

Basal body (BB) movement was recorded using a Spinning Disk-Olympus Super Resolution microscope (SD-OSR, Olympus) (Hayashi and Okada, 2015) equipped with a silicon oil-immersion objective lens (UPlanSApo 60x Sil, NA1.3), a sCMOS camera (ORCA-Flash 4.0 v2, Hamamatsu), appropriate filter sets for DAPI/FITC/TRITC, a motorized scanning deck, and an incubation chamber (37°C; 5% $CO_2$; 85% humidity) (Tokai Hit). The recording was carried out by multistage

acquisitions with 10-30 fields of view, each covering about 10 cells/field. Time intervals were 30 min for long-term recording, 15 min under nocodazole treatment, and 1-2 h under cytochalasin D treatment. Image acquisition was set to a *z*-series of 8-12 planes with a 0.5-µm distance. Immunofluorescently stained samples were imaged using a silicon oil-immersion objective lens (UPlanSApo 60x Sil, NA1.3) and ×1.6 conversion lens. The excitation light source was set to 20-40%, depending on the particular sample. All hardware was controlled with MetaMorph (Molecular Devices). The resulting 3D images were converted into 2D images by maximum intensity projection in the *z*-direction before the image analysis necessary for detecting BBs and BFs.

6.2. Thin-section electron microscopy and electron tomography with ultra-high voltage electron microscopy tomography (UHVEMT).

MTECs were fixed with 2.5% glutaraldehyde and 2% PFA at 37°C for 1 h. The following steps were based on classical methods for sample preparation for electron microscopy (Ishikawa et al., 1969). Serial sections of 90 nm were cut on an ultramicrotome (Ultracut E, Leica), and stained with uranyl acetate and lead citrate for double contrasting. Image observation was performed using a JEM 1400-Plus (JEOL). For observation using UHVEM Tomography, 700-nm-thick section specimens were observed using an ultra-high voltage electron microscope operating at 1 MeV (H-3000; Hitachi). The images were acquired at 25,000x from -60° to +60° at 2° intervals around a single axis tilt series, as described previously (Kunimoto et al., 2012).

6.3. Cilia beating.

Cilia beating was recorded using a high-speed camera (FASTCAM MC2.1; Photron) connected to an upright microscope (Zeiss Axioplan; Carl Zeiss) with ×63 objectives.

## 7. Estimation of the number of microtubules (MTs) around BBs from immunofluorescence images

Our method for estimating the amount of apical MTs has some limitations. First, MTs at the apical layer of MCCs are interspersed with hundreds of BBs. Considering

that the barrel-shaped BB consists of nine triplets of MTs (Anderson, 1972; Tateishi et al., 2013), I cannot exclude the possibility that the visualized apical MTs were mixed with artifactual signals from the BB structure. Second, the decoration of MTs with anti-tubulin antibodies hinders the visualization of individual MTs, which typically overlapped with each other in the late stage of BB alignment (Fig. 4 A in the "Alignment" pattern). Thus, the actual distribution of overlapping MTs may be underestimated. Our method presents an approximate comparison of the MTs covering the surface of MCCs at different stages, rather than the actual number of apical MTs.

Method. The algorithm to estimate the amount of MTs around BBs in a single cell has four steps: 1) extraction of the cell boundary; 2) determination of the most in-focus $z$-plane of BBs; 3) detection of MTs; 4) calculation of the surface coverage of MTs.

*Step 1: extraction of the cell boundary*

The boundary of a single cell at each $z$-slice was extracted by manually tracing the line of the Vangl1 fluorescence signal located at the cell periphery.

*Step 2: determination of the most in-focus z-plane of BBs*

The most in-focus $z$-plane of the BBs in a single cell, symbolized as $z_{\mathrm{BB}}$, was determined as the $z$-slice where the standard deviation of the fluorescence signal of Odf2 within a single cell reached its maximum value among all the $z$-slices.

*Step 3: detection of MTs*

To detect MTs, each $z$-slice of the fluorescence image $I(x, y)$ of the MTs was processed by a filter that removes background noise and enhances fibrous structures. For this purpose, a Frangi filter was used (Frangi et al., 1998).

*Step 4: calculation of the surface coverage of MTs.*

As the above probability depends on the fluorescence intensity of the original image $I$, a simple averaging of this probability over the area within a single cell would not give a value that can be used to compare the amount of MTs in cells at different stages. Thus, a further binarization of the probability map was performed to change $L(x, y)$ into the surface coverage of MTs, which is a more robust quantity for comparing the amount of MTs. This binarization was performed at each $z$-slice. To ensure the reliability of our

analysis, a different threshold $\bar{L}$ for the binarization that was computed using $n$-fold of the mean of the values of $L(x, y)$ was examined within a single cell ($n$ = 0.5 ~ 1.0). The results of the analysis did not qualitatively change as long as $n$ ranged from 0.5 to 1.0. The pixels with a value larger (or smaller) than the threshold $\bar{L}$ were treated as MTs (or background) and assigned a value of 1 (or 0). Considering that the fluorescence signal of Odf2 comes from the z-position, which is slightly higher than the BB plane (Fig. 3A), the surface coverage of MTs around BBs was calculated by averaging the values of the binarized maps over two $z$-slices located at $z = z_{\mathrm{BB}} - 2\Delta z$ and $z_{\mathrm{BB}} - 3\Delta z$, where $\Delta z(= 150\ \mathrm{nm})$ represents the distance between neighboring $z$-slices. This choice of $z$-slices enabled us to effectively remove signals from cilia.

## 8. Measurement of the apical surface area

To measure the apical surface area of MCCs, the cell boundaries in an MTEC sheet were stained with antibodies against ZO-1. The apical surface area of a single MCC was determined as the area confined by ZO-1 and measured using IMAGEJ software (National Institutes of Health, USA).

## Chapter IV. RESULTS AND DISCUSSIONS

### 1. The BB array adopts four stereotypical patterns during MCC differentiation, as revealed by long-term live imaging

In an individual MCC, BBs are generated via centrosome and deuterosome pathways, and dock to the apical membrane to generate cilia (Stubbs et al., 2012; Zhao et al., 2013; Al Jord et al., 2014). MCCs of adult mouse trachea and oviduct (Fig. S1 A) show a strikingly linear BB alignment that was similar to the MCCs of cultured mouse tracheal epithelial cells (MTECs) prepared from the GFP-centrin2 transgenic mouse trachea (Fig. 3, A and B). To study the mechanism involved in BB alignment in the apical plane of MCCs, a live-imaging system which can be used for long periods (see Materials and methods for details) was developed. Using this system, live GFP-centrin2-expressing MTECs (Higginbotham et al., 2004) (Fig. 3, C-D) were observed for 5-6 days, during which the differentiation of MCCs with beating cilia was unaffected (Fig. S1, C-F) and specimens in constant motion could be imaged.

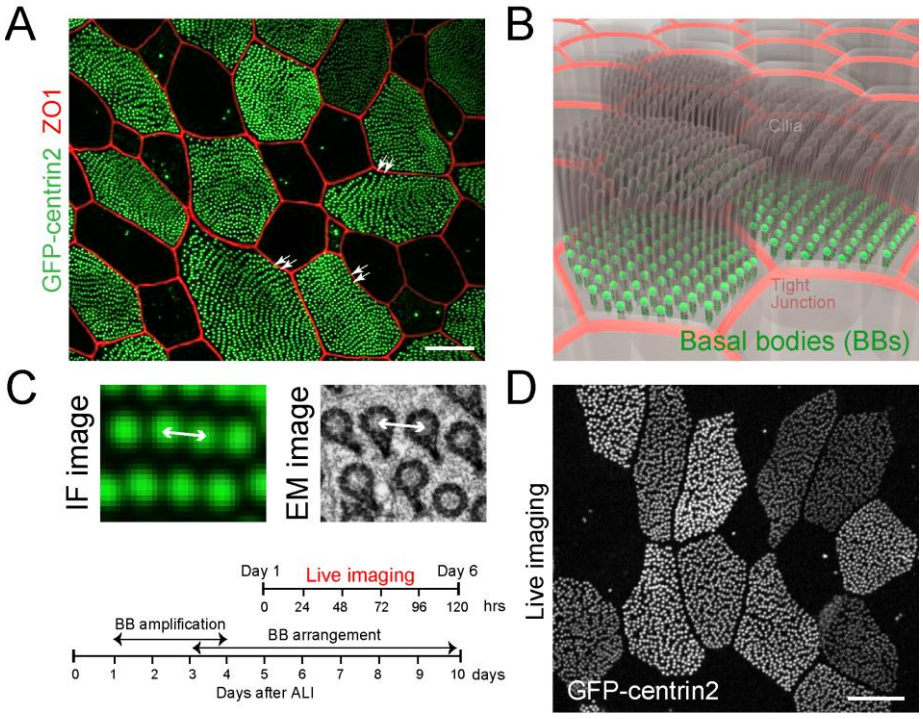


**Figure 3. Establishment of BB alignment during the MCC differentiation of MTECs revealed by long-term, high-resolution live imaging.** (A) Linear alignment of BBs (double arrows) in GFP-centrin2 MTECs at air-liquid interface (ALI) 21 days. (B) Illustration of mature polarized ciliated cells with linearly aligned BBs, depicted as green circles at the base of each cilium. (C) Immunofluorescence (IF) image of the GFP-centrin2 signal in BBs (green in top left panel), and electron micrograph (EM) image showing BBs (black rings in top right panel). Arrows: 200 nm. Timeline of live imaging and ALI culture (bottom). (D) GFP-centrin2 transgenic MTECs during live imaging. Bars, 5 μm.

Live imaging revealed that BBs first appeared as clusters with short cilia localized to the apical membrane (Fig. S1 B), which I termed the "Floret" pattern; this observation confirmed a previous report (Zhao et al., 2013). Subsequently, I found that BB "Florets" scattered over the apical cell plane ("Scatter" pattern), and neither clustered nor formed regular alignments. Then, around Day 2, three to five neighboring BBs appeared to align with each other in a side-by-side fashion to form short lines ("Partial alignment" pattern). By Day 4, these short BB lines appeared to coalesce to form longer, parallel lines ("Alignment" pattern) (Fig. 4 A). To quantitatively characterize these post-ciliogenesis BB arrays, an index of alignment ($Ia$) was introduced (Fig. S2 A), which has a high value when the BBs in a single cell are aligned (Fig. S2 B). Using $Ia$, BB array was classified into patterns as follows: <0.22 ("Floret"), 0.22-0.33 ("Scatter"), 0.33-0.43 ("Partial alignment"), and >0.43 ("Alignment") (Fig. 4 B and S2 C).

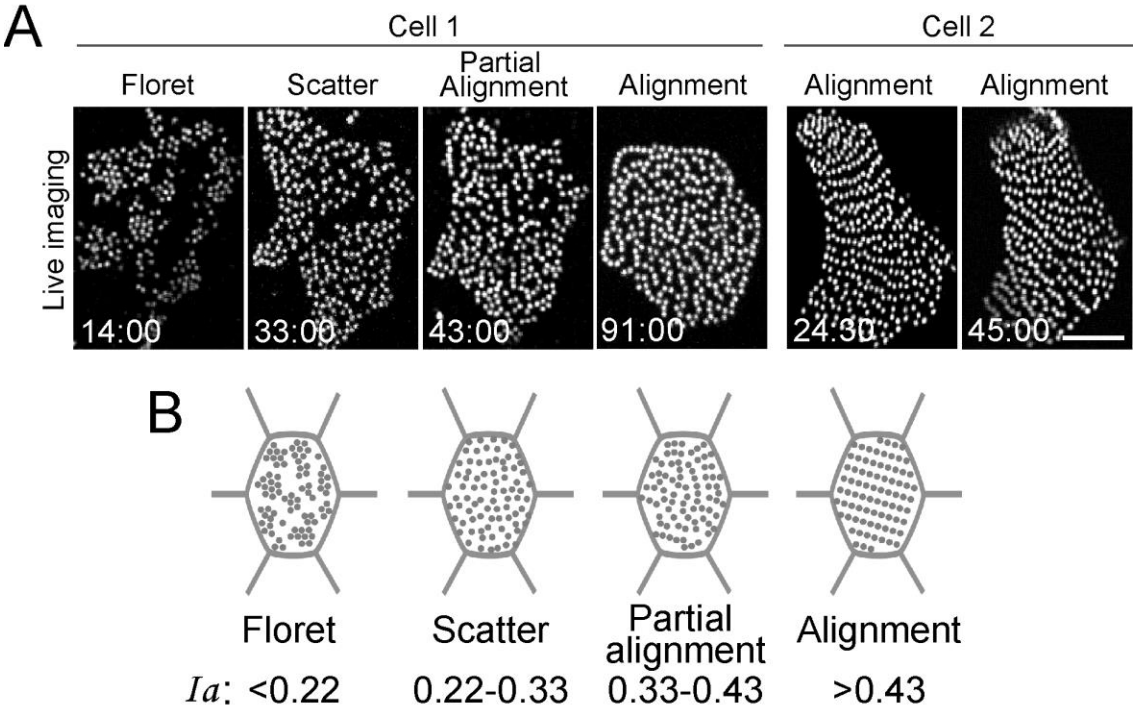


**Figure 4. BB arrays adopt four stereotypical patterns during MCCs differentiation.** (A) Live imaging of GFP-centrin2 MTECs, which exhibited four BB patterns during BB-alignment development. Time in hh:mm. (B) Schematic drawing of representative live images showing each pattern. The degree of alignment analyzed using the index of alignment ($Ia$) is shown as numeric values. Bar, 5 μm.

The spatiotemporal dynamics of individual BBs were further tracked by imaging GFP-centrin2. BBs in the "Floret" pattern moved in and out of the area of the originally assigned "Floret" cluster, and as a result, sets of BBs that later formed a line did not originate from a single "Floret" (Fig. S3 A).

Over the course of MCC culture, the $Ia$ value revealed a long-term ascending trend (Fig. S3 B), with a nearly constant number of BBs (Fig. S3 C). BBs moved most rapidly when they transitioned from the "Floret" to the "Scatter" pattern, and then gradually slowed as they approached the alignment configuration (Fig. S3 D, left). After BB alignment was established, only minor changes occurred. I also observed occasional intermittent bursts of BB velocity due to large cellular deformation caused by the cell's reconnection with a neighboring cell (Fig. S3 D, right). Taken together, the live imaging system of MCCs with quantitative analyses revealed that the BB array adopted four stereotypical patterns, from a clustering "Floret" pattern to the linear "Alignment" during MCC differentiation.

The distribution patterns of BBs determined the positions of beating cilia, the biological significance of which has been widely studied in the context of synchronization and metachronality in the ciliary beating pattern (Werner et al., 2011; Brooks and Walingford, 2014). Recent theoretical studies indicated that the pattern of ciliary positions affects the onset (Guirao and Joanny, 2007) and the efficiency of fluid transport (Osterman and Vilfan, 2011; Elgeti and Gompper, 2013) through the coordination of synchronized or metachronal ciliary beating. On the other hand, very few studies have addressed the physical mechanism underlying the establishment of the cilia positioning itself. Previous studies in *Xenopus* (Werner et al., 2011) and mouse brain (Boutin et al., 2014) demonstrated that the cytoskeleton is a common key player responsible for the formation and regulation of ciliary distribution, despite differences in the ciliary patterns of various cell types.

## 2. The establishment of BB alignment is correlated with the refinement of BB orientation

Although earlier studies (Guirao et al., 2010; Werner et al., 2011) showed that the interplay between BB position and orientation underlies proper ciliary beating in Xenopus embryonic skin and mouse brain, little is known about this process in tracheal MCCs. I examined the development of tracheal BB orientation in the course of cell

maturation and its correlation with BB alignment. By dual-color live imaging (Fig. 5) and immunostaining of Odf2 (Nakagawa et al., 2001) and centriolin (Gromley et al., 2003) which mark the positions of BBs and BFs, respectively (Fig. 6 A), I determined the orientation of each BB (Fig. 6, B and C) then estimated the degree of uniformity of BB orientation by introducing the index of orientation ($Io$). During the progressive refinement of the BB orientation over time, the $Io$ exhibited a rapid increase around air-liquid interface (ALI) days 6-7. The $Io$ values taken from all of the samples exhibit a bimodal distribution, in which a group of cells with low (<0.3) $Io$ values transitioned into cells with high (>0.7) $Io$ values within two days (Fig. 6 D). In the mouse trachea, cilia-generated directional fluid flow is absent at birth. At postnatal day 5, it is initially acquired rapidly within 48 h, and reaches a plateau at postnatal day 9 (Francis et al., 2009). Since the BB orientation indicates the beating direction of the cilia, the bimodal $Io$ values may correspond to the timing of fluid flow acquisition observed in the trachea.

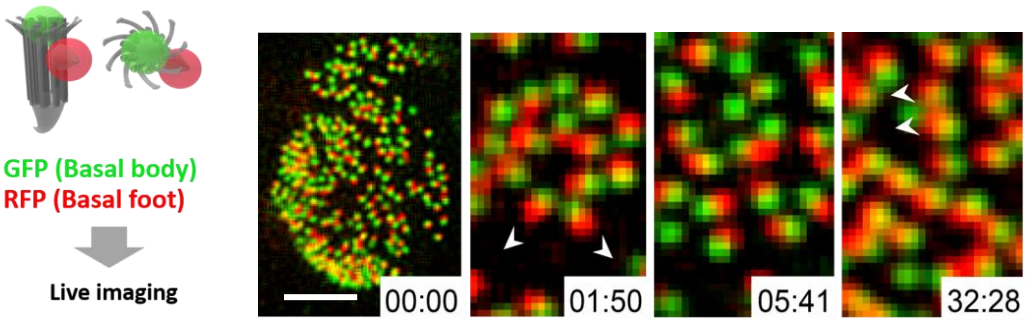


**Figure 5. Dynamics of basal body orientation demonstrated by dual-color live imaging.** Schematic drawing of fluorescence labelling of basal body and basal foot to determine the orientation of basal body (left). Dual-color live imaging in tracheal multilciliated cells. Live imaging was started when BBs are in the "Floret" pattern (00:00) with randomized BB orientation (01:50). More uniform BB orientation was coincident with formation of aligned BBs (32:28). Time in hh:mm. Bar, 5 μm.

I also found a positive correlation between the alignment and orientation of BBs (Fig. 6 E). Specifically, $Ia$> 0.25 was coincident with the increase in $Io$. When $Ia$ reached 0.4, $Io$ was high, ($Io$> 0.8). This relationship suggests a cooperative interaction between BB alignment and BB orientation, indicating that ciliary alignment may have stabilized the unidirectionality of the BBs, to enhance the function of MCCs. However, given that these analyses were based on fixed samples, the question remains whether BB alignment serves to facilitate the uniformity of BB orientations. Although dynamics of BB orientation can be visualized through dual-color live imaging of MTECs at present study (Fig. 5), analysis of long-term BB dynamics is hampered by the limitation

of RFP photostability. Thus, detailed investigations are needed to address the causal relationship between BB alignment and orientation, perhaps upon improvement of dual-color live imaging system.

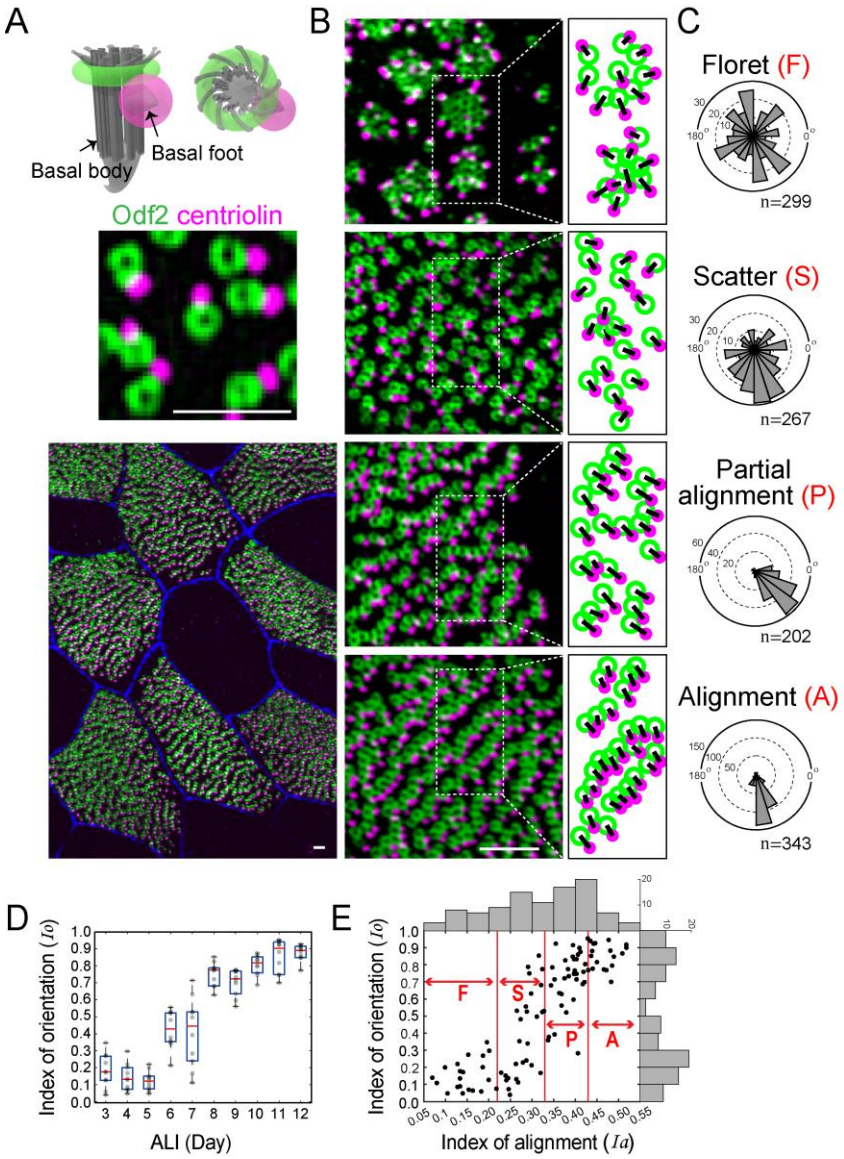


**Figure 6. Interplay between BB alignment and orientation.** (A) Schematic drawing (top) and dual-color immunofluorescence for Odf2 and centriolin (middle and bottom), which marked the BB as a ring (green) and BF as a dot (magenta), respectively. (B) Representative immunofluorescence micrographs of each pattern, with an illustration showing a line from the center of the green ring to the center of the magenta dot. (C) Angle histograms of BB directions from representative cells in each pattern. (D) Boxplot of the dependency of the index of orientation ($Io$) on the ALI day (n = 10 cells/day). (E) Correlation between the linearity of the alignments and the uniformity of the directions during MCC differentiation. Each plotted point (black circle) represents a single cell in terms of its degree of BB alignment (horizontal axis, $Ia$) and orientation (vertical axis, $Io$). Histograms of $Ia$ and $Io$ are shown by gray bars. Immunofluorescence images of 100 cells with a total of 28,501 BB-BF pairs were analyzed. Bars, 700 nm.

### 3. The apical cytoskeletons in MCCs change during BB alignment

BBs were reported to be associated with the apical cytoskeleton (Gordon, 1982; Sandoz et al., 1988; Werner et al., 2011; Antoniades et al., 2014), which may play a key role in the BB array formation. I examined the distribution of the apical actin filaments, intermediate filaments (IFs), and microtubules (MTs) in MCCs presenting the four patterns of BB arrays. For this purpose, I used a combination of super-resolution immunofluorescence microscopy and ultra-high voltage electron microscopic tomography (UHVEMT) on thick sections, and serial thin-section electron microscopy. The apical surface of MCCs turned out to contain a mixture of cytoskeletons (actin filaments, IFs, and MTs), which form a dense polymer network confined to a thin layer just underneath the apical membrane (Fig. 7-9).

Actin filaments were distributed between BBs (Fig. 7 A); these filaments are known to run mainly downward from microvilli interspersed between cilia (Chailley et al., 1989; Pan et al., 2007). They occasionally appeared to be associated with BBs and BFs, consistent with previous studies (Reed et al., 1984; Kunimoto et al., 2012) and with my electron microscopic observation of heavy meromyosin (HMM)-treated samples (Fig. 8 B). I found that IFs, which were not decorated with HMM (a standard method for distinguishing them from actin filaments), were present between BBs, surrounding them at distances of ~50–100 nm (Fig. 7 C). Closer examination of the early-stage BB pattern revealed that thick bundles of IFs frequently appeared around the BB Florets; this pattern was not reported previously (Fig. 8 A).

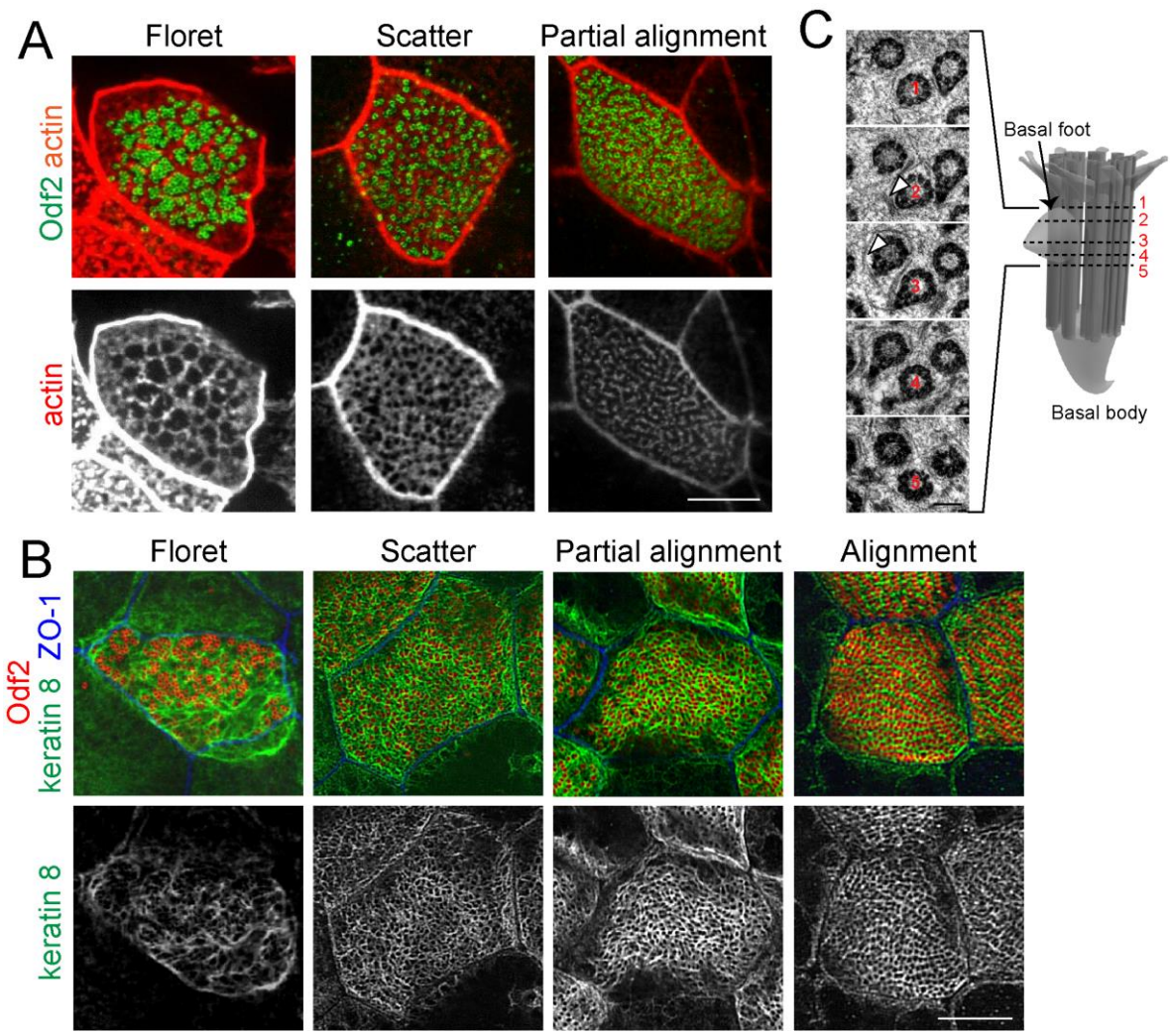


**Figure 7. Distribution of apical actin and intermediate filaments in MCCs of MTECs.** (A) Localization of apical actin using phalloidin staining. (B) Immunostained images with an anti-keratin 8 mAb. Apical keratin intermediate filaments appeared to encircle each BB in all of the BB patterns, forming exceptionally thick bundles in the "Floret" pattern. (C) Intermediate filaments visualized in serial thin-section electron micrographs taken from the lowest to the uppermost part of a BF (*z*-width: 90 nm). The intermediate filament bundles (arrowheads) were concentrated at the upper region of the BF. Bars, 5 μm (A, B); 200 nm (C).

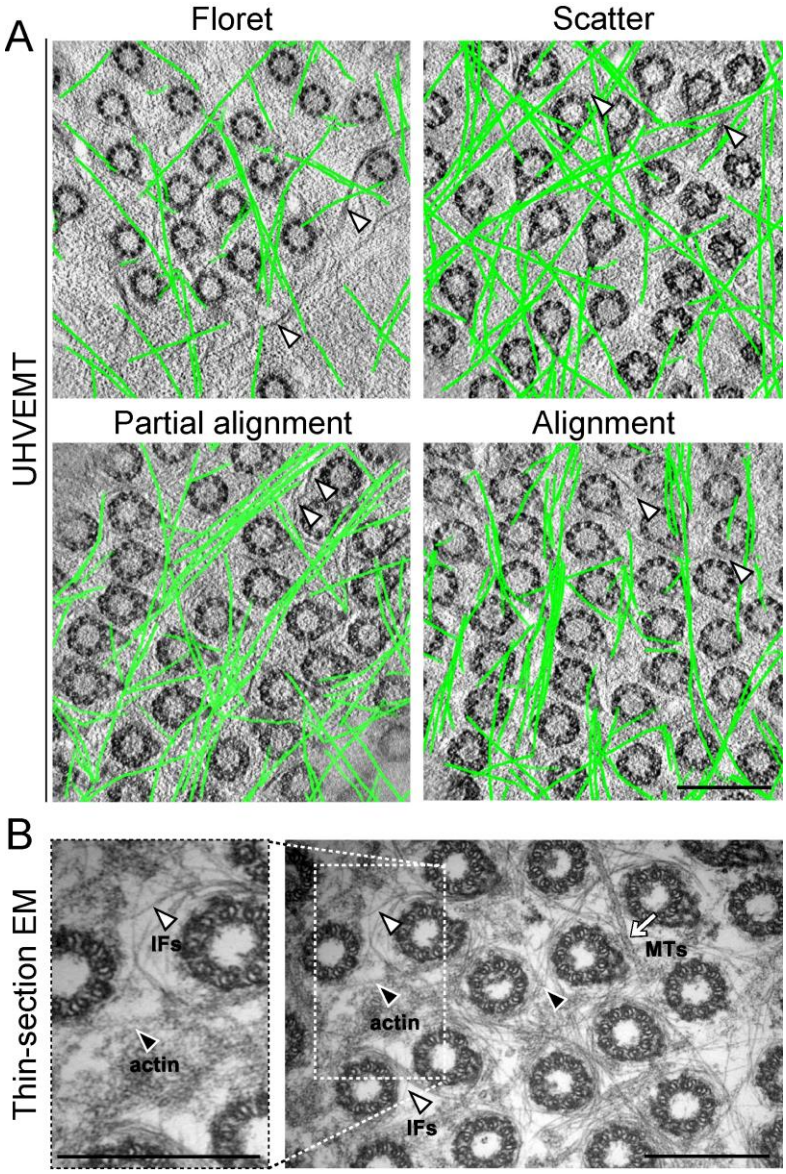


**Figure 8. Apical cytoskeletons in MTECs revealed by ultra-high voltage electron microscopic tomography (UHVEMT) and thin-section electron microscopy (EM).** (A) Selected tomographic slices showing the pattern-specific distribution of microtubules (green lines) and intermediate filaments (arrowheads). Note the thick bundles of intermediate filaments in the "Floret" pattern. Microtubule lines were drawn from a 3D reconstruction and superimposed on a single cross section. (B) Thin-section EM image of HMM-treated MTECs at ALI 28 days (right panel). Actin filaments are decorated with HMM showing the typical arrowhead patterns (black arrowheads), while intermediate filaments are not decorated (white arrowheads). Microtubules (arrow). High magnification image of actin filaments decorated with HMM (left panel). Bars, 500 nm.

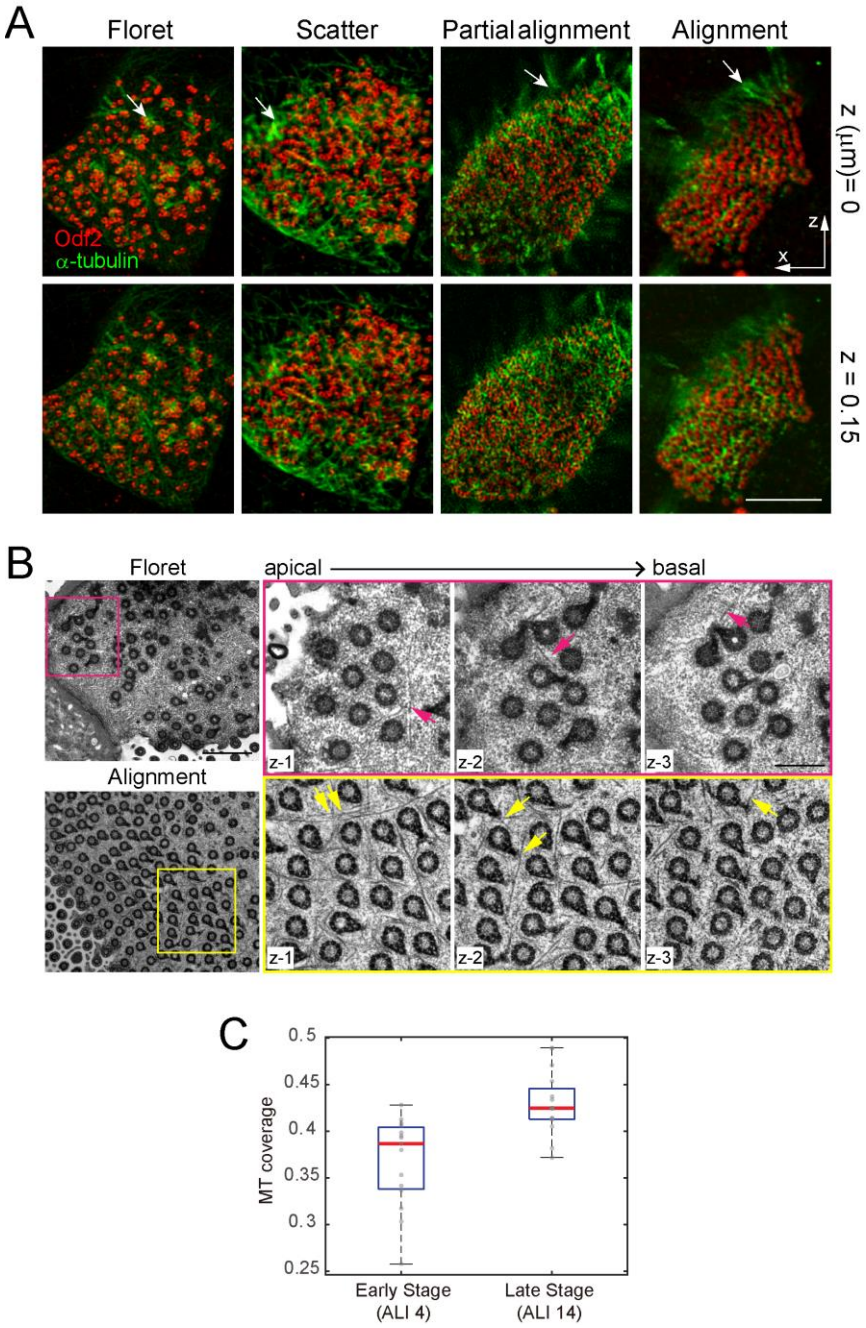


**Figure 9. Distribution of apical microtubules in MTECs revealed by super-resolution confocal microscopy and serial thin-section electron microscopy.** (A) Networks of microtubules (MTs) for each BB pattern are shown in three successive *z*-slice images using super-resolution confocal microscopy. Fluorescently labeled apical MTs (α-tubulin) slightly below the Odf2 plane were separated from the ciliary MT signals (arrow) at *z*-slices +0.15 μm. The MT density increased from the "Floret" to the "Scatter", "Partial alignment", and "Alignment" patterns during development. (B) Apical MTs in MTECs visualized by a series of thin-section electron micrographs (*z*-width: 90 nm). Pink arrows indicate MTs associating with BFs in the "Floret" pattern. Yellow arrows show MTs binding to BFs and parallel MT bundles. (C) MT coverage measured at two different stages: Early Stage (ALI 4 days, n = 15) and Late Stage (ALI 14 days, n = 16). The MT coverage at the two stages was significantly different by Welch's t test (*P* value $1.8\times10^{-4} < 0.01$). Bars, 5 μm (A); 500 nm (B).

The number and distribution of MTs increased during the progressive reorganization of BB alignment. The MT density around BBs increased during the transition from the “Floret” to “Scatter” pattern (Fig. 8 A and 9 A). In the “Floret” pattern, only a few MTs associated with BFs in the apical cortical region of MCCs. In the “Scatter”, “Partial alignment”, and “Alignment” patterns, significant numbers of MTs, distributed nearly in parallel to the apical membrane, were associated with BFs (Fig. 8 A and 9 B). During the transition toward the “Alignment” pattern, increasing numbers of MTs appeared to form parallel bundles through mutual interactions (Fig. 8 A and 9 C). Thus, in the apical cortical layer containing the BBs, cytoskeletal structures were densely distributed with some of them mutually interacting with BBs. Among these structures, the MTs were prominently aligned to promote BB alignment.

**4. Actin and MT depolymerization affects BB alignment**

To explore the role of the cytoskeleton in BB alignment, I treated MTECs with the actin depolymerizing agent cytochalasin D. I found that the alignment of BBs was disturbed and the spacing between BBs was decreased (Fig. 10 A), as well as dissociation of BBs from the apical membrane (Fig. 10 B). These observations are consistent with previous findings that actin plays an organizing role in BB spacing and apical docking (Pan et al., 2007; Werner et al., 2011; Antoniades et al., 2014). In addition, I noticed that cytochalasin D at a concentration that effectively disrupted the apical actin network, induced a shrinkage of the apical surface area in MCCs (Fig. 10 C) without significantly affecting the BB number (Fig.10 D), resulting in a narrowing of the spacing between BBs. This observation suggests an alternative way that actin determines BB positioning; not only by making interconnections at the proper distance between the BBs (Werner et al., 2011), but also by regulating the total area of the apical cell surface. A role for actin in regulating the apical surface area of MCCs was reported previously (Sedzinski et al., 2016).

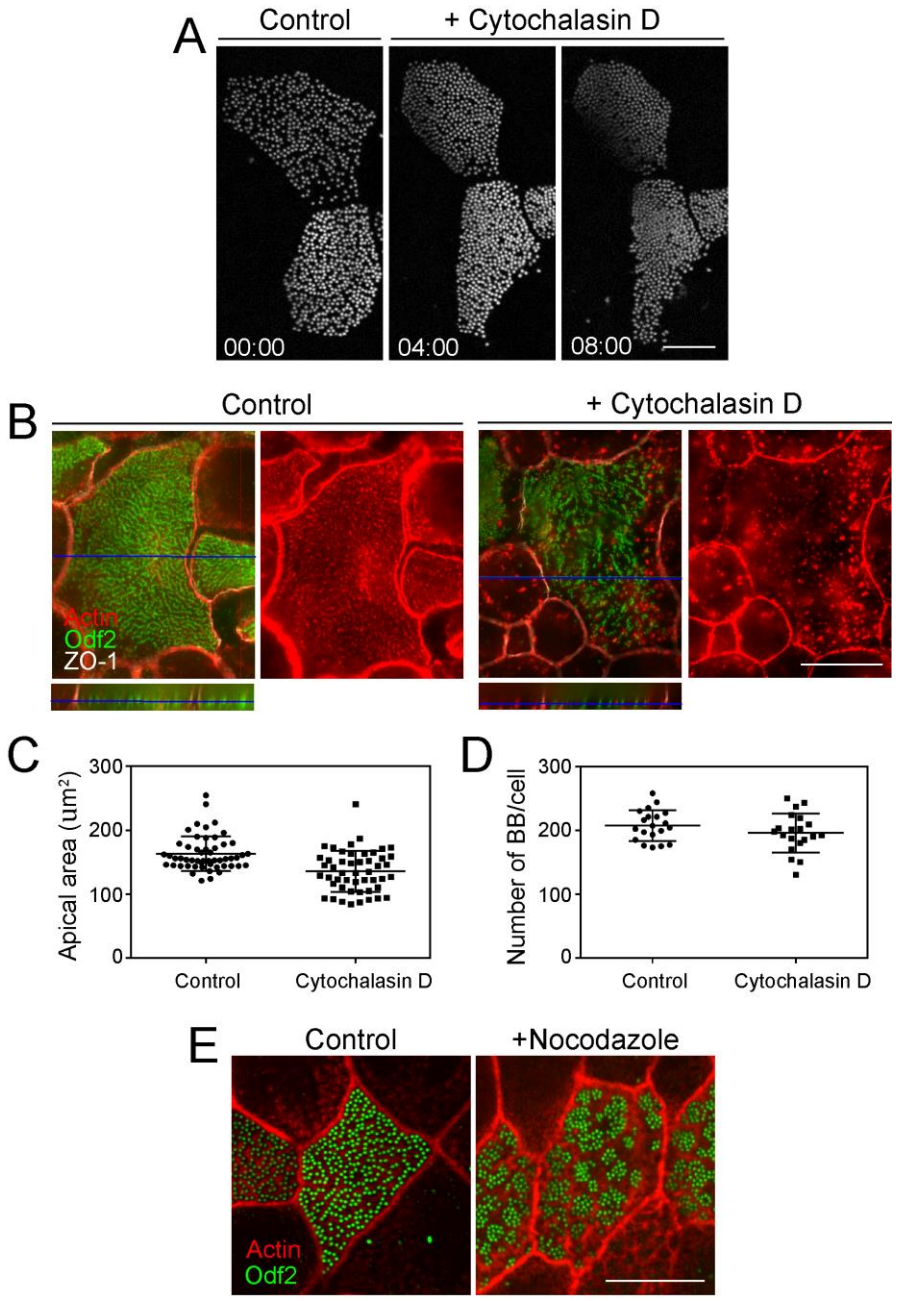


**Figure 10. Effects of drug treatment on BB arrays and apical cytoskeleton.** (A) BB behavior by actin perturbation using cytochalasin D in GFP-centrin2 MTECs at ALI 9 days under live imaging. Loss of apical actin disturbed the BB spacing, which changed to a minimum distance between BBs followed by a loss of BB attachment to the apical surface. Time in hh:mm. (B) The effect of cytochalasin D on the localization of apical actin was verified in wild-type MTECs at ALI 14 under normal incubation. BBs were found in the cytoplasm when apical actin was disrupted. The XZ plane of the apical surface of MCCs is shown. (C) Apical area of MCCs measured using the cell boundary marker ZO-1. Cytochalasin D treatment apparently induced apical constriction, whereby the area of the apical surface was reduced (n=49, control; n=53, treatment). (D) Number of BBs after cytochalasin D treatment. No significant difference between control and treatment (n=20). (E) Organization of actin filaments after nocodazole treatment. Bars, 5 μm.

MT depolymerization with nocodazole showed distinct effects on BB arrays. In GFP-centrin2-expressing MCCs in which the BBs were already aligned, nocodazole disturbed the BB alignment, resulting in clusters of BBs resembling the “Floret” pattern (Fig. 11 A). The clusters of BBs were retained under an extended duration of MT depolymerization. On the other hand, washing out nocodazole remarkably returned the nocodazole-induced “Floret”-like pattern to the “Partial alignment” pattern, suggesting that transitions between these states are reversible and MT-dependent (Fig. 11, A and S4 A). Furthermore, the response to nocodazole treatment differed depending on the state of BB alignment. The clusters of BBs were clearer on earlier-stage cells (Fig. 11 B) and the change in their $Ia$ occurred more rapidly (Fig S4 B). Because fewer MTs were associated with BBs in the “Floret” pattern (Fig. 8 A), depolymerizing MTs in the earlier-stage cells would presumably lead to a more severe phenotype.

In nocodazole-treated cells, I confirmed that the immunofluorescent intensity of MTs was reduced (Fig. 11 C), whereas the actin filament distribution was relatively unaffected (Fig. 10 E). The networks of keratin IFs were profoundly altered by nocodazole, including the formation of filament bundles surrounding the “Floret”-like BBs (Fig. 11, D and E). Similar morphological changes in IFs in response to shear stress have been reported in cultured human alveolar A549 epithelial cells (Flitney et al., 2009).

I also followed changes in BB orientation during nocodazole treatment using dual-color immunofluorescence of GFP-centrin2 and centriolin for BBs and BFs, respectively (Fig. 11 F). I found that the coordination of the BB orientation was disturbed by MT perturbation, similar to the case in the “Floret” pattern in BB arrays in the earliest phase of differentiation. Nocodazole washout restored the coordination of BB orientation.

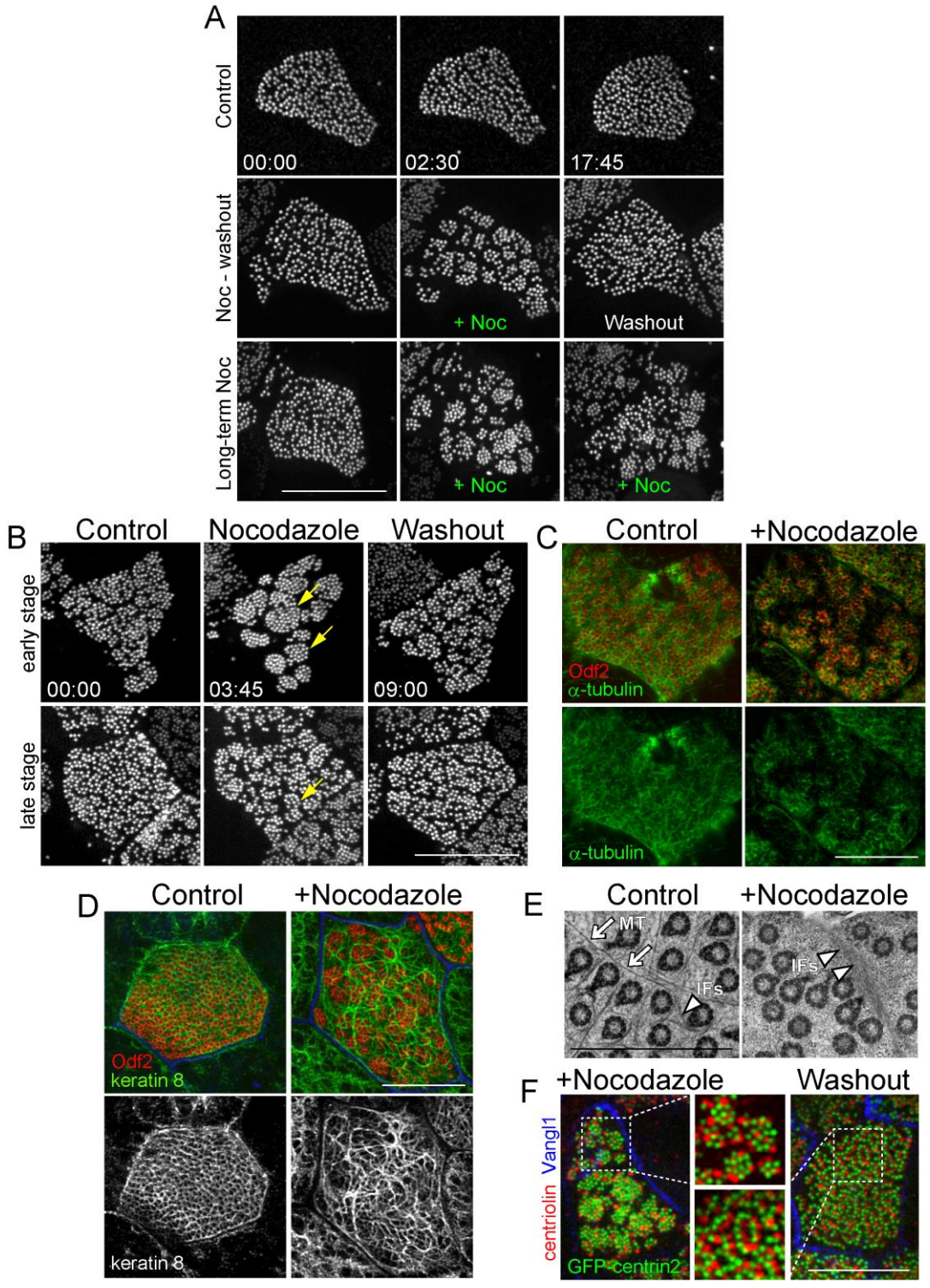


**Figure 11. Requirement for microtubules in establishing and maintaining BB alignment.** (A) Effects of nocodazole on the BB patterns in GFP-centrin2 MTECs. Comparison of three different conditions of nocodazole treatment. Time in hh:mm. (B) Different responses to nocodazole treatment in early- versus late-stage cells. More prominent clustering (arrows) appeared in the early-stage cells (top row) in the presence of nocodazole compared to late-stage cells (bottom row). Time in hh:mm. (C) Apical microtubules in MTECs at ALI 6 days treated with 6.6 μM nocodazole for 2 h showed a lower intensity of $\alpha$-tubulin staining compared to non-treated MTECs. (D) Immunostained images with an anti-keratin 8 mAb after nocodazole treatment revealed prominent keratin bundling. (E) Nocodazole treatment

altered the normal IF network visualized by EM. Coincident with the depolymerization of microtubules (MT, white arrows), intermediate filaments (IFs, white arrowheads) formed thick bundles surrounding individual BBs clusters. (F) The impaired BB pattern induced by nocodazole treatment was a "Floret"-like pattern with random BB directions. Insets are magnified regions. Bars, 10 μm (A-D, F), 1 μm (E).

While these findings revealed that MTs play a critical role in the linear alignment of BB arrays from the "Floret" to the "Partial alignment"/"Alignment" patterns, and in the simultaneous coordination of BB orientation, I could not exclude the participation of actin filaments and IFs in maintaining the proper BB arrays. The fact that MT disruption also affected the organization of keratin IFs suggests that the cytoskeletons interact with each other. To explore this possibility, I examined the localization of plectin, a major IF-based cross-linker protein that can facilitate physical interactions between MTs, IFs, and actin (Svitkina et al., 1996; Wiche et al., 2015). Although a previous study showed that the transcription level of plectin is upregulated in the MCCs of MTECs (Hoh et al., 2012), the spatial distribution of the plectin in the cells was not examined. I found that the plectin distribution closely corresponded to that of keratin IFs (Fig. S5 A) and partly co-localized with MTs (Fig. S5 B). These findings support the idea that the three types of cytoskeletons associate with each other through cross linkers like plectin, and thus could act cooperatively to drive the dynamic motion of BBs.

## 5. Loss of BFs from the BBs causes undirected BB movement and perturbs the establishment of the "Alignment" pattern

Previous work in our laboratory (Kunimoto et al., 2012) revealed the requirement of Odf2-based BFs for functional mucociliary clearance. In the tracheal MCCs of Odf2 mutant (*Odf2*$^{\Delta Ex6,7\Delta Ex6,7}$) mice, the absence of BFs impaired the regularity of the BB arrays and the polarized organization of apical MTs (Fig. 2). However, the dynamic process of the BB array development in these mutant mice was unknown. To resolve this issue, I next examined MTECs prepared from GFP-centrin2-transgenic Odf2 mutant mice generated in this study, in which the BBs lack BFs.

I detected BBs in the typical "Floret" pattern in the *Odf2*$^{\Delta Ex6,7\Delta Ex6,7}$ GFP-centrin2 MTECs at the earliest stage of MCCs differentiation (Fig. 12 A). Subsequently, and in sharp contrast to wild-type GFP-centrin2-MTECs (Fig. 3 A and 4 A), GFP-centrin2 in the BBs in *Odf2*$^{\Delta Ex6,7\Delta Ex6,7}$MTECs revealed only a partial progression of the "Floret" pattern to the "Scatter" pattern, and no progression to the "Partial alignment" or

"Alignment" pattern. The dynamic behavior of the BBs was further specified by determining the *Ia*s, which remained low in the *Odf2*$^{\Delta Ex6,7/\Delta Ex6,7}$GFP-centrin2 MTECs (Fig. S4 C). In addition, tracheas from these mutant mice showed disorganized BB alignment (Fig. 12 B). These findings strongly suggest that BF-associated cytoskeletal structures, such as MTs, play important roles in BB alignment.

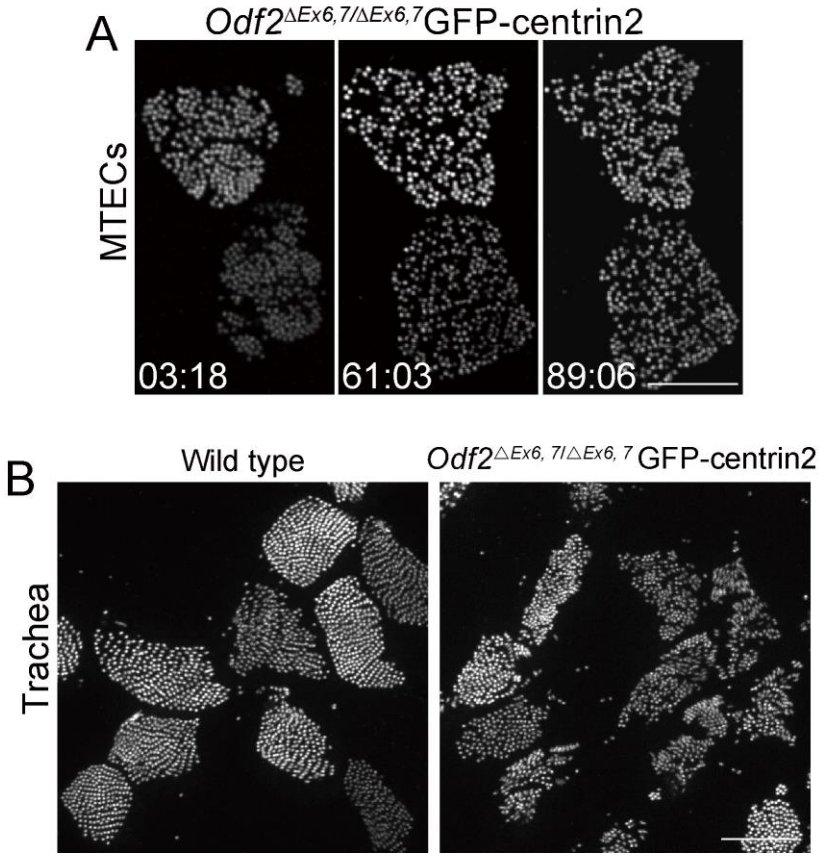


**Figure 12**. **BFs are indispensable for BB alignment.** (A) Live imaging of *Odf2*$^{\Delta Ex6,7/\Delta Ex6,7}$ GFP-centrin2 MTECs in which the BBs lack BFs. In the absence of BFs, BBs transitioned from the "Floret" to "Scatter" pattern, but failed to develop into the "Alignment" pattern. Time in hh:mm. (B) Disorganized BB array observed in the *Odf2*$^{\Delta Ex6,7/\Delta Ex6,7}$GFP- centrin2 tracheal cells lacking BFs. The trachea was isolated from mice at postnatal 24 days. Bars, 10 μm.

## Chapter V. CONCLUSION

The dynamics, sequential changes in ciliary patterns that occurred during the maturation of mouse tracheal MCCs were quantified in this study. The process occurred through four stereotypical changes in the BB array. These changes in BB patterns were positively correlated with the refinement of ciliary orientation, indicating that ciliary alignment may have stabilized the unidirectionality of the BBs, to enhance the function of MCCs. Furthermore, this study demonstrated that the genetic loss of BFs in *Odf2*$^{\Delta Ex6,7/\Delta Ex6,7}$ MTECs prevented BBs from achieving the "Alignment" pattern, and drug-induced apical MT disruption caused the "Alignment" pattern to change to a "Floret-like" pattern, suggesting that a self-organization mechanism involving the associated apical cytoskeleton could give rise to these patterns.

Although different BB distributions in the apical layer have been reported in various organ systems, some common mechanisms may be involved in the formation and regulation of BB organization. The present study provides a new framework for understanding apical cytoskeletal function as exemplified in multiciliated epithelial cells. Such an autonomous, self-organizing mechanism with or without a coupled cell-signaling system may play critical roles in various morphogenetic processes in both single and multicellular systems.

The effects of other factors, such as cytoskeletal polarity (Shimada et al., 2006; Vladar et al., 2012), regulation by PCP signaling (Seifert and Mlodzik, 2007; Park et al., 2008; Mitchell et al., 2009; Boutin et al., 2014), and hydrodynamic coupling between cilia (Mitchell et al., 2007; Guirao et al., 2010; Matsuo et al., 2013) need to be examined in future studies.

## References


Al Jord, A., A.-I. Lemaître, N. Delgehyr, M. Faucourt, N. Spassky, and A. Meunier. 2014. Centriole amplification by mother and daughter centrioles differs in multiciliated cells. *Nature*. 516:104–107. doi:10.1038/nature13770.

Anderson, R.G. 1972. The three-dimensional structure of the basal body from the rhesus monkey oviduct. *J. Cell Biol.* 54:246–265. doi:10.1083/jcb.54.2.246.

Antoniades, I., P. Stylianou, and P.A. Skourides. 2014. Making the connection: ciliary adhesion complexes anchor basal bodies to the actin cytoskeleton. *Dev. Cell*. 28:70–80. doi:10.1016/j.devcel.2013.12.003.

Boutin, C., P. Labedan, J. Dimidschstein, F. Richard, H. Cremer, P. André, Y. Yang, M. Montcouquiol, A.M. Goffinet, and F. Tissir. 2014. A dual role for planar cell polarity genes in ciliated cells. *Proc. Natl. Acad. Sci. U. S. A.* 111:E3129–E3138. doi:10.1073/pnas.1404988111.

Brooks, E.R., and J.B. Wallingford. 2014. Multiciliated Cells. *Curr. Biol.* 24:R973–R982. doi:10.1016/j.cub.2014.08.047.

Chailley, B., G. Nicolas, and M.C. Lainé. 1989. Organization of actin microfilaments in the apical border of oviduct ciliated cells. *Biol. Cell*. 67:81–90.

Delgehyr, N., Sillibourne, J., Bornens, M. 2005. Microtubule nucleation and anchoring at the centrosome are independent processes linked by ninein function. *J Cell Sci*. 118:1565–75.

Dirksen, E.R. 1971. Centriole morphogenesis in developing ciliated epithelium of the mouse oviduct. *J Cell Biol.* 51:286–302.

Elgeti, J., and G. Gompper. 2013. Emergence of metachronal waves in cilia arrays. *Proc. Natl. Acad. Sci. U. S. A.* 110:4470–4475. doi:10.1073/pnas.1218869110.

Flitney, E.W., E.R. Kuczmarski, S.A. Adam, and R.D. Goldman. 2009. Insights into the mechanical properties of epithelial cells: the effects of shear stress on the assembly and remodeling of keratin intermediate filaments. *FASEB J.* 23:2110–2119. doi:10.1096/fj.08-124453.

Francis, R.J.B., B. Chatterjee, N.T. Loges, H. Zentgraf, H. Omran, and C.W. Lo. 2009. Initiation and maturation of cilia-generated flow in newborn and postnatal mouse airway. *Am. J. Physiol. Lung Cell. Mol. Physiol.* 296:L1067–L1075. doi:10.1152/ajplung.00001.2009.

Frangi, A.F., W.J. Niessen, K.L. Vincken, and M.A. Viergever. 1998. Multiscale vessel enhancement filtering. *Med. Image Comput. Comput. Interv. MICCAI'98. Lect. Notes Comp Sci.* 1496:130–137.

Gordon, R.E. 1982. Three-dimensional organization of microtubules and microfilaments of the basal body apparatus of ciliated respiratory epithelium. *Cell Motil.* 2:385–391.

Gromley, A., A. Jurczyk, J. Sillibourne, E. Halilovic, M. Mogensen, I. Groisman, M. Blomberg, and S. Doxsey. 2003. A novel human protein of the maternal centriole is required for the final stages of cytokinesis and entry into S phase. J. Cell Biol. 161:535–545. doi:10.1083/jcb.200301105

Gueron, S., Levit-Gurevich, K., Liron, N., and Blum, J. 1997. Cilia internal mechanism and metachronal coordination as the result of hydrodynamical coupling. *Proc. Natl. Acad. Sci. USA*. 94: 6001–6006.

Guillot, C., and T. Lecuit. 2013. Mechanics of epithelial tissue homeostasis and morphogenesis. *Science.* 340:1185–1189. doi:10.1126/science.1235249.

Guirao, B., and J.-F. Joanny. 2007. Spontaneous creation of macroscopic flow and metachronal waves in an array of cilia. *Biophys. J.* 92:1900–1917. doi:10.1529/biophysj.106.084897.

Guirao, B., A. Meunier, S. Mortaud, A. Aguilar, J.-M. Corsi, L. Strehl, Y. Hirota, A. Desoeuvre, C. Boutin, Y.-G. Han, Z. Mirzadeh, H. Cremer, M. Montcouquiol, K. Sawamoto, and N. Spassky. 2010. Coupling between hydrodynamic forces and planar cell polarity orients mammalian motile cilia. *Nat. Cell Biol.* 12:341–350. doi:10.1038/ncb2040.

Hayashi, S., and Y. Okada. 2015. Ultrafast superresolution fluorescence imaging with spinning disk confocal microscope optics. *Mol. Biol. Cell*. 26:1743–1751. doi:10.1091/mbc.E14-08-1287.

Higginbotham, H., S. Bielas, T. Tanaka, and J.G. Gleeson. 2004. Transgenic mouse line with green-fluorescent protein-labeled Centrin 2 allows visualization of the centrosome in living cells. *Transgenic Res.* 13:155–164. doi:10. 1023/B:TRAG. 0000026071.41735.8e.

Hirota, Y., A. Meunier, S. Huang, T. Shimozawa, O. Yamada, Y.S. Kida, M. Inoue, T. Ito, H. Kato, M. Sakaguchi, T. Sunabori, M.-A. Nakaya, S. Nonaka, T. Ogura, H. Higuchi, H. Okano, N. Spassky, and K. Sawamoto. 2010. Planar polarity of multiciliated ependymal cells involves the anterior migration of basal bodies regulated by non-muscle myosin II. *Development*. 137:3037–3046. doi:10. 1242/dev.050120.

Hoh, R.A., T.R. Stowe, E. Turk, and T. Stearns. 2012. Transcriptional program of ciliated epithelial cells reveals new cilium and centrosome components and links to human disease. *PLoS One*. 7:e52166. doi:10.1371/journal.pone.0052166.

Hoyer-Fender, S. 2010. Centriole maturation and transformation to basal body. *Semin. Cell Dev*. Biol. 2010; 21:142–147.

Ioannou, A., Santama, N., and Skourides, P.A. 2013. Xenopus laevis nucleotide binding protein 1 (xNubp1) is important for convergent extension movements and controls ciliogenesis via regulation of the actin cytoskeleton. *Dev. Biol*. 380: 243–258.

Ishikawa, H., R. Bischoff, and H. Holtzer. 1969. Formation of arrowhead complexes with heavy meromyosin in a variety of cell types. *J. Cell Biol.* 43:312–328. doi:10.1083/jcb.43.2.312.

Ishikawa, H., A. Kubo, S. Tsukita, and S. Tsukita. 2005. Odf2-deficient mother centrioles lack distal/subdistal appendages and the ability to generate primary cilia. *Nat. Cell Biol.* 7:517–524. doi:10.1038/ncb1251.

Kitajiri, S., T. Miyamoto, A. Mineharu, N. Sonoda, K. Furuse, M. Hata, H. Sasaki, Y. Mori, T. Kubota, J. Ito, M. Furuse, and S. Tsukita. 2004. Compartmentalization established by claudin-11-based tight junctions in stria vascularis is required for hearing through generation of endocochlear potential. *J. Cell Sci.* 117:5087–5096. doi:10.1242/jcs.01393.

Kobayashi, T. and Dynlacht, B.D. 2011. Regulating the transition from centriole to basal body. *J. Cell Biol.* 193:435–444.

Kunimoto, K., Y. Yamazaki, T. Nishida, K. Shinohara, H. Ishikawa, T. Hasegawa, T. Okanoue, H. Hamada, T. Noda, A. Tamura, S. Tsukita, and S. Tsukita. 2012. Coordinated ciliary beating requires Odf2-mediated polarization of basal bodies via basal feet. *Cell*. 148:189–200. doi:10.1016/j.cell.2011.10.052.

Leigh, M. W., Pittman, J. E., Carson, J. L., Ferkol, T. W., Dell, S. D., Davis, S. D., Knowles, M. R., Zariwala, M. A. 2009. Clinical and genetic aspects of primary ciliary dyskinesia/Kartagener syndrome. *Genet Med*. 11: 473-87.

Matsuo, M., A. Shimada, S. Koshida, Y. Saga, and H. Takeda. 2013. The establishment of rotational polarity in the airway and ependymal cilia: analysis with a novel cilium motility mutant mouse. *Am. J. Physiol. Lung Cell. Mol. Physiol.* 304:L736–L745. doi:10.1152/ajplung.00425.2012.

Marshall, W.F. and Kintner, C. 2008. Cilia orientation and the fluid mechanics of development. *Curr. Opin. Cell Biol*. 20: 48–52.

Mirzadeh, Z., Y.-G. Han, M. Soriano-Navarro, J.M. García-Verdugo, and A. Alvarez-Buylla. 2010. Cilia organize ependymal planar polarity. *J. Neurosci.* 30:2600–2610. doi:10.1523/JNEUROSCI.3744-09.2010.

Mitchell, B., R. Jacobs, J. Li, S. Chien, and C. Kintner. 2007. A positive feedback mechanism governs the polarity and motion of motile cilia. *Nature*. 447:97–101. doi:10.1038/nature05771.

Mitchell, B., J.L. Stubbs, F. Huisman, P. Taborek, C. Yu, and C. Kintner. 2009. The PCP Pathway Instructs the Planar Orientation of Ciliated Cells in the Xenopus Larval Skin. *Curr. Biol.* 19:924–929. doi:10.1016/j.cub.2009.04.018.

Moritz, M,. Braunfeld, MB., Sedat, JW., Alberts, B., Agard, DA. 1995. Microtubule nucleation by γ-Tubulin-containing rings in the centrosome. *Nature*. 378:638–40.

Nakagawa, Y., Y. Yamane, T. Okanoue, S. Tsukita, and S. Tsukita. 2001. Outer dense fiber 2 is a widespread centrosome scaffold component preferentially associated with mother centrioles: its identification from isolated centrosomes. Mol. Biol. Cell. 12:1687–1697. doi:citeulike-article-id:8295986.

Osterman, N., and A. Vilfan. 2011. Finding the ciliary beating pattern with optimal efficiency. *Proc. Natl. Acad. Sci. U. S. A.* 108:15727–32. doi:10.1073/pnas.1107889108.

Pan, J., Y. You, T. Huang, and S.L. Brody. 2007. RhoA-mediated apical actin enrichment is required for ciliogenesis and promoted by Foxj1. *J. Cell Sci.* 120:1868–1876. doi:10.1242/jcs.005306.

Park, T.J., B.J. Mitchell, P.B. Abitua, C. Kintner, and J.B. Wallingford. 2008. Dishevelled controls apical docking and planar polarization of basal bodies in ciliated epithelial cells. *Nat. Genet.* 40:871–879. doi:10.1038/ng.104.

Quintyne, NJ., Gill, SR., Eckley, DM., Crego, CL., Compton, DA., Schroer, TA. 1999. Dynactin is required for microtubule anchoring at centrosomes. *J Cell Biol*. 147:321–34

Reed, W., J. Avolio, and P. Satir. 1984. The cytoskeleton of the apical border of the lateral cells of freshwater mussel gill: structural integration of microtubule and actin filament-based organelles. *J. Cell Sci.* 68:1–33.

Rodriguez-Boulan, E., and I.G. Macara. 2014. Organization and execution of the epithelial polarity programme. *Nat. Rev. Mol. Cell Biol.* 15:225–242. doi:10.1038/nrm3775.

Sandoz, D., B. Chailley, E. Boisvieux-Ulrich, M. Lemullois, M.C. Laine, and G. Bautista-Harris. 1988. Organization and functions of cytoskeleton in metazoan

ciliated cells. *Biol. Cell*. 63:183–193. doi:http://dx.doi.org/.

Satir, P. and Dirksen, E. R. 2011. Function-structure correlations in cilia from mammalian respiratory tract. In Comprehensive Physiology. Pollock, D. M., editor. American Physiology Association, Bethesda. 473–494. doi: 10.1002/cphy.cp030115.

Satir, P. and Christensen, S.T. 2007. Overview of structure and function of mammalian cilia. *Annu. Rev. Physiol*. 69: 377–400.

Sedzinski, J., E. Hannezo, F. Tu, M. Biro, and J.B. Wallingford. 2016. Emergence of an Apical Epithelial Cell Surface In Vivo. *Dev. Cell*. 36:24–35. doi:10. 1016/j.devcel.2015.12.013.

Seifert, J.R.K., and M. Mlodzik. 2007. Frizzled/PCP signalling: a conserved mechanism regulating cell polarity and directed motility. *Nat. Rev. Genet.* 8:126–138. doi:10.1038/nrg2042.

Shi, D., F. Usami, K. Komatsu, S. Oka, T. Abe, T. Uemura, and T. Fujimori. 2016. Dynamics of planar cell polarity protein Vangl2 in the mouse oviduct epithelium. *Mech. Dev.* doi:10.1016/j.mod.2016.05.002.

Shimada, Y., S. Yonemura, H. Ohkura, D. Strutt, and T. Uemura. 2006. Polarized transport of Frizzled along the planar microtubule arrays in Drosophila wing epithelium. *Dev. Cell*. 10:209–222. doi:10.1016/j.devcel.2005.11.016.

Sorokin, S.J. 1968. Reconstructions of centriole formation and ciliogenesis in mammalian lungs. *Cell. Sci*. 3: 207–230.

Steinman, R.M. 1968. An electron microscopic study of ciliogenesis in developing epidermis and trachea in the embryo of *Xenopus laevis*. *Am. J. Anat*. 122:19–55.

Stubbs, J.L., E.K. Vladar, J.D. Axelrod, and C. Kintner. 2012. Multicilin promotes centriole assembly and ciliogenesis during multiciliate cell differentiation. *Nat. Cell Biol.* 14:140–147. doi:10.1038/ncb2406.

Svitkina, T.M., A.B. Verkhovsky, and G.G. Borisy. 1996. Plectin sidearms mediate interaction of intermediate filaments with microtubules and other components of the cytoskeleton. *J. Cell Biol.* 135:991–1007.

Tamura, A., and S. Tsukita. 2014. Paracellular barrier and channel functions of TJ claudins in organizing biological systems: advances in the field of barriology revealed in knockout mice. *Semin. Cell Dev. Biol.* 36:177–185. doi:10. 1016/j.semcdb.2014.09.019.

Tateishi, K., Y. Yamazaki, T. Nishida, S. Watanabe, K. Kunimoto, H. Ishikawa, and S. Tsukita. 2013. Two appendages homologous between basal bodies and centrioles

are formed using distinct Odf2 domains. *J. Cell Biol.* 203:417–425. doi:10.1083/jcb.201303071.

Turk, E., A.A. Wills, T. Kwon, J. Sedzinski, J.B. Wallingford, and T. Stearns. 2015. Zeta-Tubulin Is a Member of a Conserved Tubulin Module and Is a Component of the Centriolar Basal Foot in Multiciliated Cells. *Curr. Biol.* 25:2177–2183. doi:10.1016/j.cub.2015.06.063.

Vladar, E.K. and T. Stearns. 2007. Molecular characterization of centriole assembly in ciliated epithelial cells. *J Cell Biol*. 178:31-42. doi:10.1083/jcb.200703064.

Vladar, E.K., R.D. Bayly, A.M. Sangoram, M.P. Scott, and J.D. Axelrod. 2012. Microtubules enable the planar cell polarity of airway cilia. *Curr. Biol.* 22:2203–2212. doi:10.1016/j.cub.2012.09.046.

Wallingford, J.B.2010. Planar cell polarity signaling, cilia and polarized ciliary beating. *Curr. Opin. Cell Biol*. 22: 597–604.

Wanner, A., Salathé, M., and O'Riordan, T.G. 1996. Mucociliary clearance in the airways. *Am. J. Respir. Crit. Care Med*. 154: 1868–1902.

Werner, M.E., P. Hwang, F. Huisman, P. Taborek, C.C. Yu, and B.J. Mitchell. 2011. Actin and microtubules drive differential aspects of planar cell polarity in multiciliated cells. *J. Cell Biol.* 195:19–26. doi:10.1083/jcb.201106110.

Wiche, G., S. Osmanagic-Myers, and M.J. Castañón. 2015. Networking and anchoring through plectin: a key to IF functionality and mechanotransduction. *Curr. Opin. Cell Biol.* 32:21–29. doi:10.1016/j.ceb.2014.10.002.

You, Y., E.J. Richer, T. Huang, and S.L. Brody. 2002. Growth and differentiation of mouse tracheal epithelial cells: selection of a proliferative population. *Am. J. Physiol. Lung Cell. Mol. Physiol.* 283:L1315–L1321. doi:10. 1152/ajplung.00169.2002.

Zhao, H., L. Zhu, Y. Zhu, J. Cao, S. Li, Q. Huang, T. Xu, X. Huang, X. Yan, and X. Zhu. 2013. The Cep63 paralogue Deup1 enables massive de novo centriole biogenesis

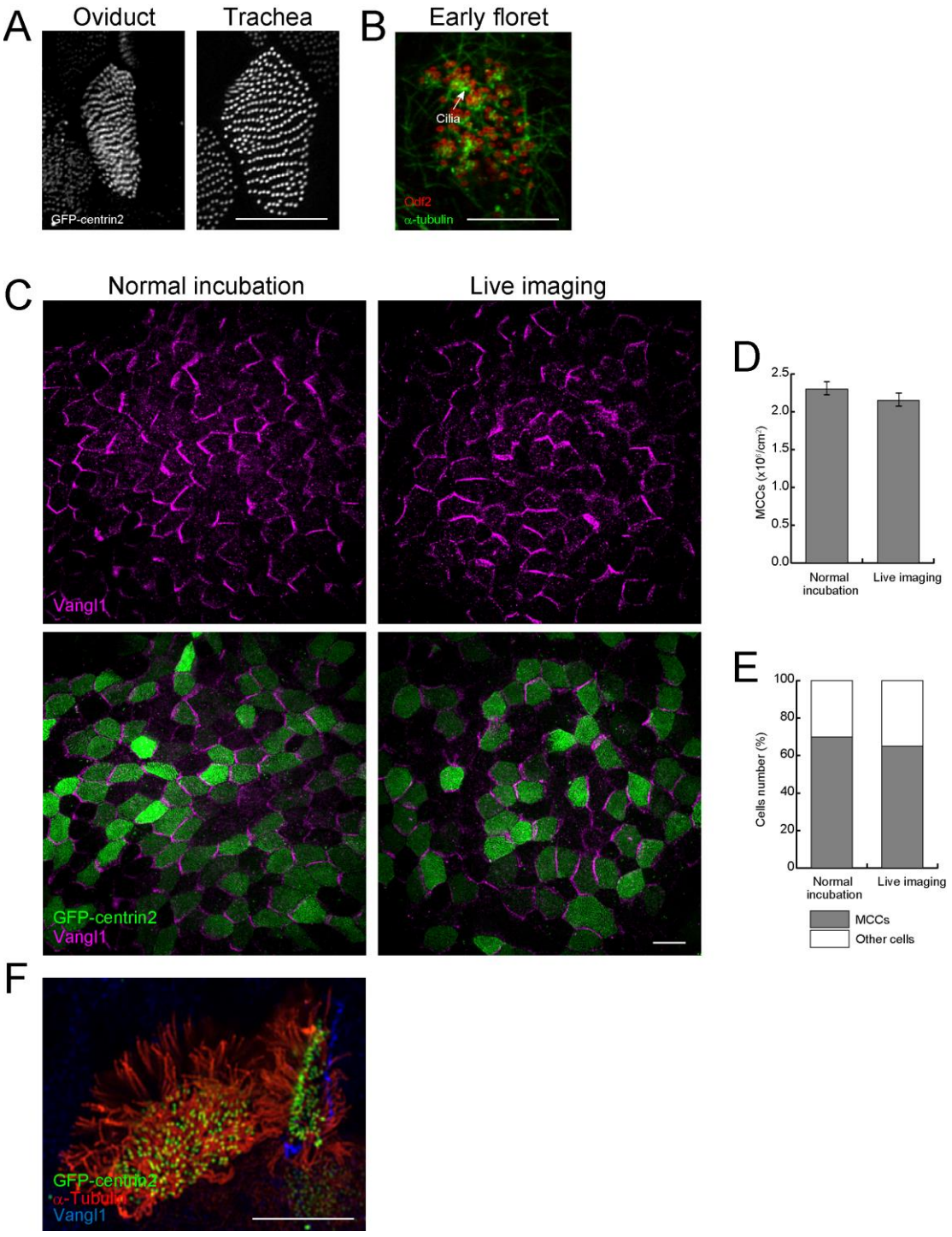


**Supplemental Figure 1. Basal body alignment in tissue and verification of MTEC conditions after live imaging.** (A) Linear alignment of basal bodies (BBs) in the oviduct and tracheal cells of adult GFP-centrin2 transgenic mice. (B) Cilia (arrow), labeled with α-tubulin, started to elongate from the apical surface in the "Floret" pattern. (C-F) Verification of MTEC conditions after live imaging. (C) MTECs maintained at ALI for ~5 days to promote ciliogenesis were transferred to a microscope stage for live imaging and submerged in medium. After live imaging Day 5, the MTECs were fixed and stained with the indicated antibodies. Vangl1 localization in MTECs showed no difference between the live-imaged and control (ALI 10 days) cells. (D) The number of MCCs and (E) the proportions of MCCs and other cells were comparable between the live-imaged and control MTECs. (F) The cilia morphology and ciliary beating of the live-imaged cells were normal. Bars, 10 μm.

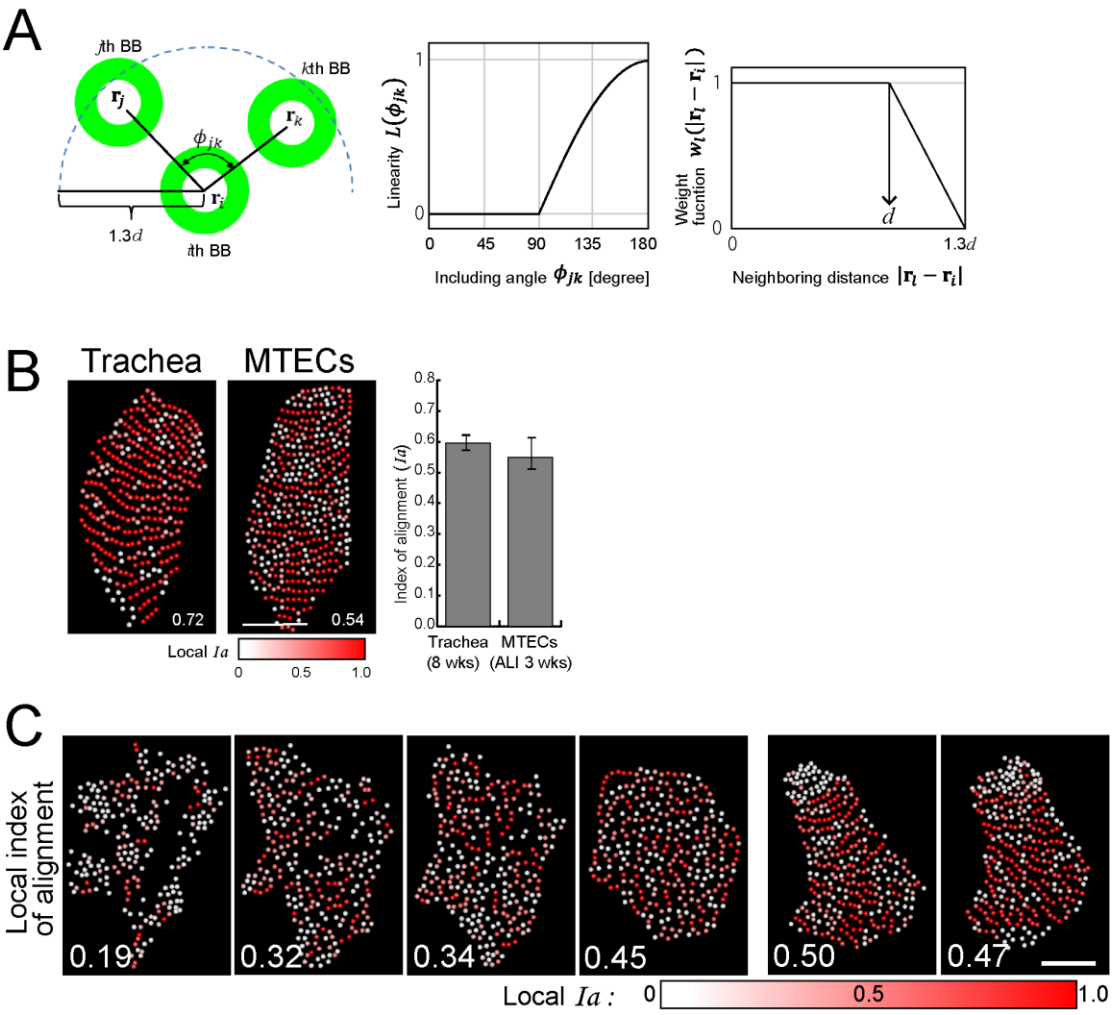


**Supplemental Figure 2. Analysis of basal body alignment.** (A) Method for calculating $Ia$. The BBs within a distance of $1.3d$ (where $d$ is the BB diameter) are considered neighbors of the $i$th BB (left). The linearity $L$ around the $i$th BB is evaluated based on the included angle $\phi_{jk}$ made by the two lines $\overline{\mathbf{r}_i\mathbf{r}_j}$ and $\overline{\mathbf{r}_i\mathbf{r}_k}$ (center), while the weight $w$ is calculated using the distance between the $i$th BB and its neighboring BBs (right). (B) Color map of the local index of alignment ($Ia$) value in the adult tracheal cells and MTECs at air liquid interface ALI 22 days. Bar graph shows the average $Ia$ in the GFP-centrin2-derived tracheal cells and MTECs (n>3). (C) Color map of the local index of alignment ($Ia$) value calculated from Figure 3 (A). Bars, 5 μm.

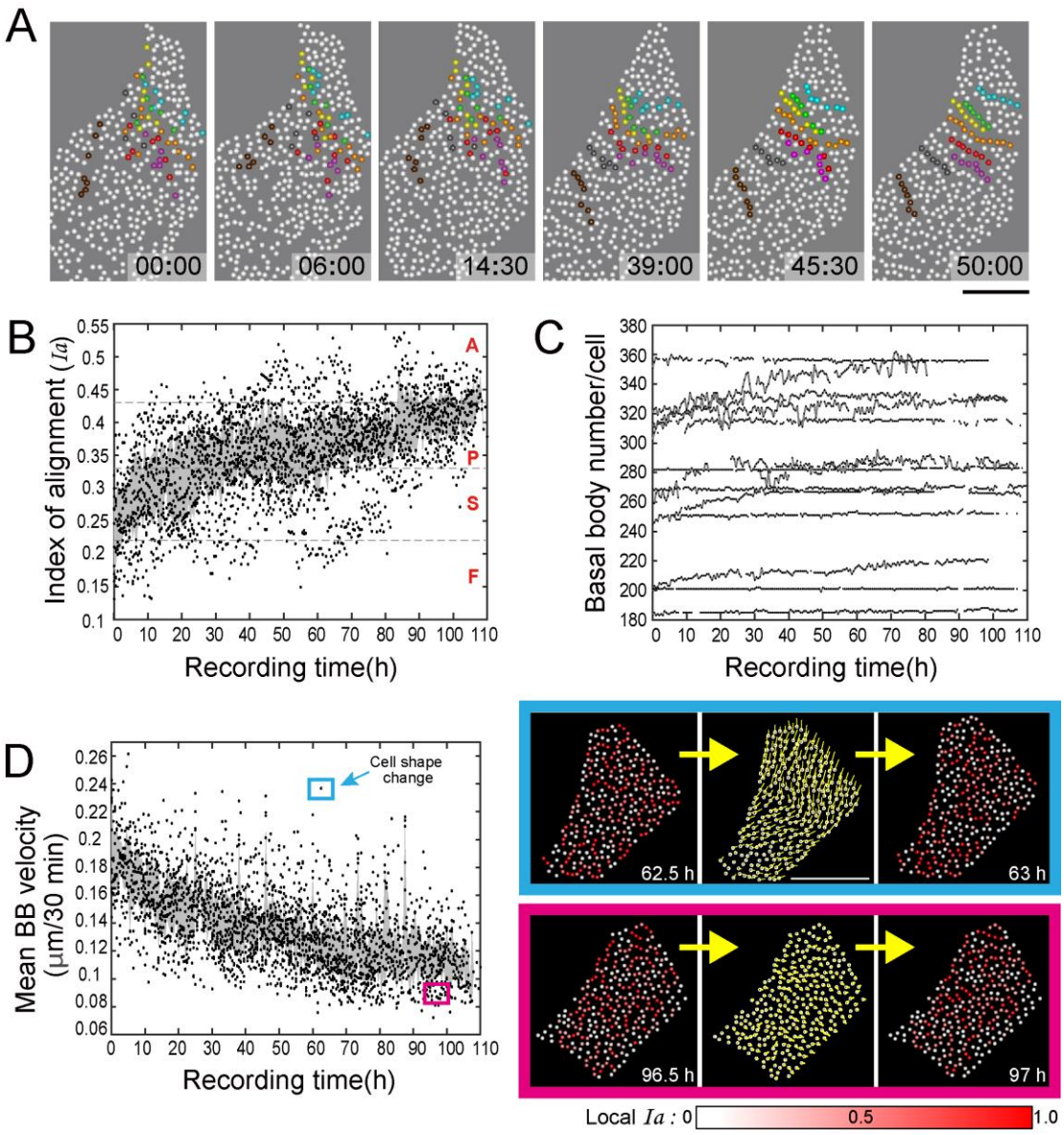


**Supplemental Figure 3**. **Tracing the spatiotemporal dynamics of BBs**. (A) Migratory tracks of individual BBs recruited into 8 alignments indicated by different colors. Time in hh:mm. (B) Time course of BB alignment evaluated using $Ia$. A: "Alignment", P: "Partial alignment", S: "Scatter", F: "Floret". Horizontal dashed lines indicate boundaries that separate different patterns. (C) Number of BBs in individual cells during the development of BB alignment. The number of BBs remained almost constant during the stereotyped patterns of BB development. Note that apparent small fluctuations in BB numbers were caused by the fact that part of a cell was occasionally out-of-focus during the live imaging. (D) Temporal change in the velocities of BBs averaged within single cells (left). BB motion drifting due to cell stretching (right, blue box) and BB motion under no significant cell deformation (right, pink box). Quantitative analyses in (B-D) were performed using the same cells (n = 14). Gray regions in (B) and (D) represent the 25-75% percentile band at each time point. Bar, 5 μm (A), 10 μm (D).

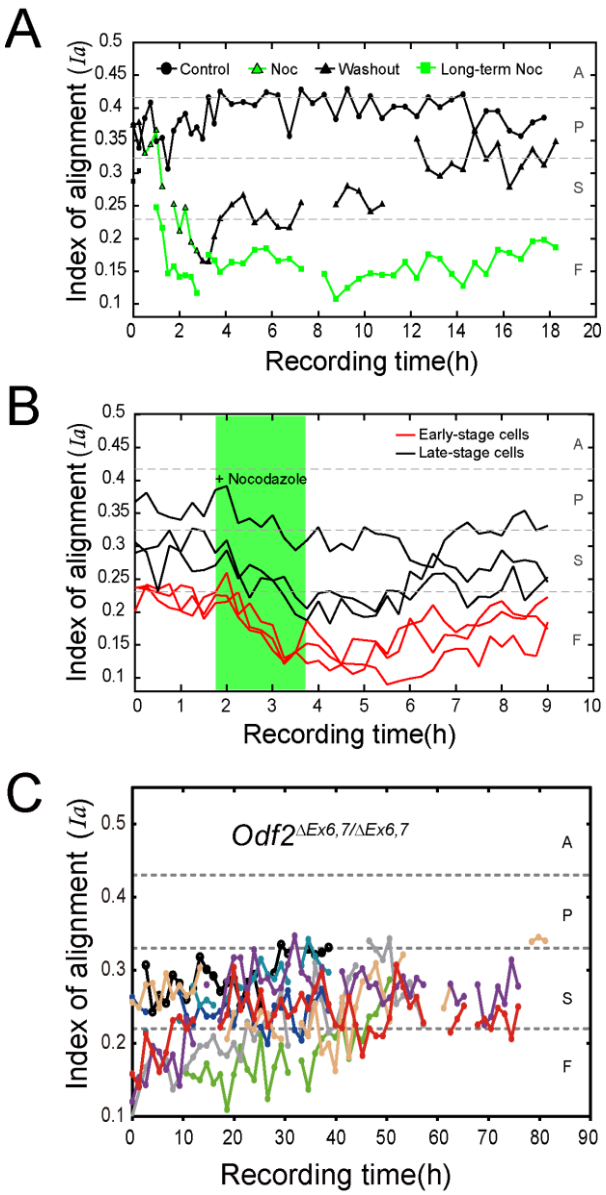


**Supplemental Figure 4. Measurement of index of alignment in nocodazole treated cells and Odf2 mutant cells.** (A) Measurement of $Ia$ from cells shown in Figure 11 (A). No treatment (black circles), short-term treatment (green triangles) followed by washout (black triangles), and long-term treatment (green squares). A: "Alignment", P: "Partial alignment", S: "Scatter", F: "Floret". (B) Temporal changes in $Ia$ in early- and late-stage cells, shown in Figure 11 (B). Black lines represent late-stage cells (those belong to "Scatter/Partial alignment" pattern), and red lines show early-stage cells (those belong to "Floret" pattern). Green region indicates the period of nocodazole treatment. (C) The $Ia$ of eight cells from *Odf2*$^{\Delta Ex6,7/\Delta Ex6,7}$GFP-centrin2 MTECs shown in Figure 12 (A) remained low. A: "Alignment", P: "Partial alignment", S: "Scatter", F: "Floret".

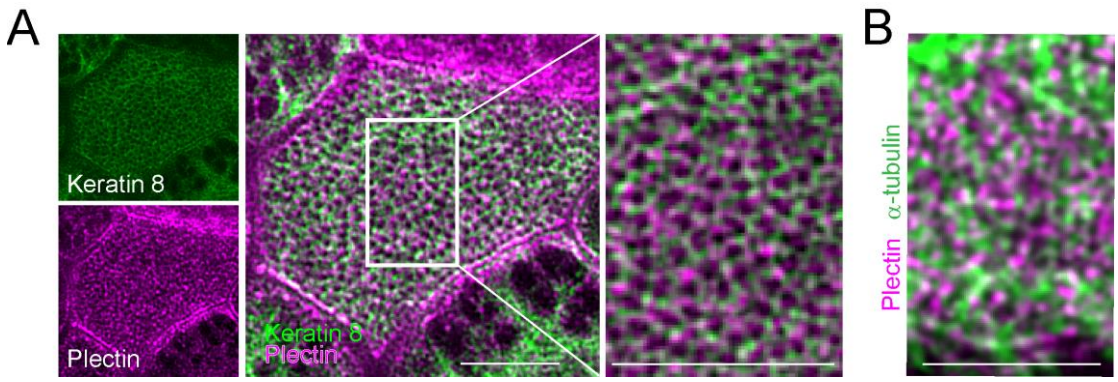


**Supplemental Figure 5. Detection of the cytoskeletal cross-linker plectin in MTEC multiciliated cells.** (A) A fluorescently labeled anti-plectin antibody was readily detectable in MTECs at ALI 14 days. Plectin distribution strongly overlapped with keratin 8. (B) Single *z*-slice of a confocal image also shows plectin partly co-localized with α-tubulin.